Scanning Tunneling Microscopy of self-organized semiconductor quantum dots

A dissertation submitted to the
SWISS FEDERAL INSTITUTE OF TECHNOLOGY
LAUSANNE

for the degree of
Doctor in Sciences

presented by
Carlos de Jesús Manzano García
M. Sc., CINVESTAV, México
of Mexican nationality

examining board:
Prof. K. Kern, thesis director
Priv. Doz. Dr. D. Grützmacher,
Prof. E. Kapon,
Dr. P. Kratzer,

Lausanne, EPFL
2004

Abstract

This thesis is committed to the study of nanometer scale surface processes involved in the formation and evolution of self-organized semiconductor quantum dots. The aim is to contribute to a better understanding of the mechanisms influencing the final shape and composition of as-grown quantum dots, as well as those exposed to post-growth treatments (annealing and overgrowth), since these determine in great extent the optic and electronic characteristics of the quantum dots.

The whole investigation conducted in the frame of this dissertation was performed by means of in-situ STM measurements of quantum dots formed on the two most important model semiconductor systems, InAs/GaAs(001) and Ge/Si(001).

InAs/GaAs(001) quantum dots grown at high temperature and extremely low flux are investigated. The detailed analysis of high resolution STM images of these dots allows for first time the exact determination of their shape, as well as the precise identification of the facets orientation composing them. This shape is in excellent agreement with recent theoretical predictions, proving that the chosen deposition conditions are close to thermodynamic equilibrium.

The low-temperature GaAs overgrowth of these QDs is investigated during the initial stages (1-30 ML). Two regimes appear to dominate the capping, an initial partial dissolution of the QDs followed by a true overgrowth. The generality of this picture is confirmed by experiments done at different overgrowth rates. The observed dependence of the QD evolution on the GaAs flux demonstrates that the observed phenomena are kinetically driven and that the two regimes are governed by different atomic processes. It is noticed that during the overgrowth, the dot dissolution is accompanied by a shape transformation. The different transition shapes adopted by

the overgrown dot are clearly identified and a physical interpretation of the atomistic mechanism producing these shape changes is presented.

The pyramid-to-dome transition in the Ge/Si(001) system is investigated. The precise pathway of the transition is determined from nanometer-resolution images and can be described as a selective overgrowth of pyramid islands. Based on experimental data and on atomistic arguments derived from recent theoretical investigations, a simple model that captures the essential features of the transformation is also presented.

By analyzing both quantum dot semiconductor systems, we demonstrate that the existence (and coexistence) of only two well-defined families of islands (small-shallow and large-steep) as well as the transformations that these undergo during the embedding-passivation process, are general features and do not depend on the particular material system.

Résumé

Cette thèse est consacrée à l'étude des processus surfaciques à l'échelle nanométrique impliqués dans la formation et l'évolution de quantum dots semiconducteurs auto-organisés. L'objectif est de contribuer à une meilleure compréhension des mécanismes influençant la forme et la composition finales de quantum dots non encapsulé, ainsi que ceux soumis à des traitements post-croissance (recuit et reprise de croissance), puisque celles-ci déterminent dans une large mesure les caractéristiques optiques et électroniques des quantum dots.

L'ensemble du travail de recherche de cette thèse a été effectué au moyen de mesures STM in situ de quantum dots formés sur les deux plus importants systèmes modèles de semiconducteurs, InAs/GaAs(001) et Ge/Si(001).

Des quantum dots obtenus par croissance InAs/GaAs(001) à haute température et faible flux ont été étudiés. L'analyse détaillée d'images STM haute résolution de ces quantum dots permet pour la première fois la détermination exacte de leur forme, ainsi que l'identification précise de l'orientation des facettes qui les composent. La forme observée est en excellent accord avec de récentes prédictions théoriques, prouvant que les conditions de dépôt choisies sont proches de l'équilibre thermodynamique.

La croissance à basse température de GaAs sur ces quantum dots est étudiée dans ses premières étapes (1-30 ML). Deux régimes semblent dominer l'encapsulement, une partielle dissolution initiale des quantum dots suivie d'une véritable croissance. La généralité de cette image est confirmée par des expériences effectuées à différents taux de croissance. La dépendance de l'évolution des quantum dots avec le flux de GaAs démontre que les phénomènes observés sont contrôlés cinématiquement et que les deux régimes sont régis par des processus atomiques différents. Il est à noter

iv

que, pendant la croissance, la dissolution du quantum dot est accompagnée d'une transformation de la forme de celui-ci. Les différentes formes transitoires adoptées par le quantum dot pendant cette croissance ont été clairement identifiées et une interprétation physique du mécanisme atomique donnant lieu à ces changements de forme est présentée.

La transition pyramide-dôme dans le système Ge/Si (001) a été étudiée. Le cheminement précis de cette transition a été déterminé par des images de résolution nanométrique et peut être décrite en terme de croissance sélective des îles de forme pyramidale. A partir de données expérimentales et d'arguments à l'échelle atomique déduits de résultats théoriques récents, un modèle simple et qui capture les traits essentiels de cette transformation est également présenté.

Par l'analyse de ces deux systèmes de quantum dots semiconducteurs, nous démontrons l'existence (et la coexistence) de seulement deux familles définies de quantum dot (petit-peu profond " small-shallow " et grand-escarpé " large-steep ") ainsi que le fait que les transformations subies par ces dernières pendant le procédé d'encapsulation et de passivation sont générales et ne dépendent pas du matériau du système.

Contents

Chapter 1

Introduction

The term quantum dot (QD) refers to a crystalline structure whose electronic states resemble those of an atom rather than those of the bulk crystal [1]. Atomic-like features appear whenever the Fermi wavelength of charge carriers becomes comparable with the structural dimensions of nanostructures in which they are confined. For semiconductors this happens in the sub 100 nm range while, in the case of metals, sizes smaller than 10 nm are required. As a consequence, semiconductor structures able to confine electrons and holes within 50-100 nm, can be considered as quantum dots or, as is also often said, as artificial atoms.

There are two basic technological motivation for the study of QDs. On one side they could be used as ultimate components in standard electronic devices, since thanks to their nanometer size, they could be extremely fast and they would allow an ultra-low energy dissipation. On the other hand in such systems quantum-mechanical effects are so important that devices with fundamentally new properties could be obtained. Although at present there is not any commercial device based on quantum dots, the number of proposed applications is steadily increasing. In this perspective, the fact that QDs absorb and emit light in a very narrow spectral range, could be of importance in the construction of more efficient and more controllable optoelectronic devices like semiconductor lasers, infrared detectors, etc [2, 3, 4]. The strong quantization of electron energy, with parameters suitable for laser action and the large separation between the energy levels, will probably allow QD-based lasers to work

at higher temperatures and lower injection currents [5]. The small dimensions and the possibility of dense packing into QD-matrices, could also permit to use them as computer memory media of huge capacity. In addition, an intriguing challenge whose investigation started just recently, is the possibility of employing QDs for developing quantum information devices [6, 7, 8]. Because of its atom-like features, a single quantum dot is also considered as a candidate system for the generation of single photons [9, 10]. Moreover, as soon as the problem of producing photons in a controlled manner will be solved, the quantum dot could become a suitable data transmission source for photon-based quantum cryptography and quantum computing [11, 12, 13].

The carrier confinement, responsible for the quantum mechanical effects exploited by all the envisaged applications, is achieved by embedding a small bandgap material QD within a larger bandgap matrix. Such kind of confinement was already used during the initial attempts of building lithographically defined QDs. In this case a quantum well provided a confining potential along the growth direction, while the lateral confinement was supplied by an electrostatically induced potential barrier [14]. The drawback of such a lithographic approach is represented by the series of complex and highly-resource demanding processing steps that are involved in the QD definition. Moreover the required resolution and accuracies are at the limits of the present technology, so that the sizes of QDs typically obtained by this method result in energy separations between electron sublevels that require the use of cryogenic temperatures.

An alternative method for producing semiconductor QDs is represented by self-organization. This approach takes advantage from the natural tendency of a strained, heteroepitaxial thin film to roughen and in some cases to form 3D islands. Particularly interesting for the realization of QDs is the so-called Stranski-Krastanow growth mode in which islanding takes place after the formation of a few monolayer-thick planar film. Although the nucleation of islands in lattice-mismatched heteroepitaxy has been studied for many decades, it was only recently established that such 3D islands can remain epitaxially coherent with the substrate, i.e., free of dislocations [15]. Dislocation-free islands have been observed for a variety of epilayer-substrate combi-

nations, comprising group IV-IV, II-VI, and III-V semiconductors [16, 17, 18]. In each case, in-situ growth techniques such as molecular beam epitaxy or chemical-vapor deposition are used to obtain the requisite ultraclean conditions and an accurate control of the deposition parameters. With these techniques a flux of atoms or molecules is sent to a surface held at high temperature. After diffusing across the surface, these species arrange themselves in a continuous epitaxial layer (commonly called wetting layer), that is generally under compressive strain, since it has to match the smaller lattice of the substrate. After the film has reached a critical thickness, faceted, coherent 3D islands begin to nucleate, acting as an alternative strain-relief mechanism to the formation of dislocations. While the island bases must be strained to match the substrate, the upper portion of the island can elastically relax towards its bulk lattice parameter.

Because of statistical fluctuations and kinetic limitations during growth, these self-assembled islands are usually not very uniform in size, shape and spacing, posing severe limits for device applications. Typical values for the size distribution widths are in the 5-20% range [19], although recently widths as small as 2% have been reported for specific material systems and growth conditions [20]. For the same reasons, the dots usually show a random in-plane arrangement when grown on a flat substrate. Moving from these random arrays to a lattice-like ordering would allow to exploit novel and fascinating properties of QD systems that are tied to the electronic or photonic quantum coupling within the array [21]. Spatial ordering allows also precise addressing and subsequent processing for single dot applications. Different attempts to induce spontaneous long-range ordering have been carried out, representative examples are prepatterning methods which exploit the dependence of atomic diffusion on the different surface orientations and techniques that make use of strain fields induced by buried 3D islands, since these can lead to lateral ordering and size homogenization during the epitaxial growth of QD superlattices [16]).

In the last years, research on self-organized QDs has greatly intensified, involving a large number of academic and industrial research groups around the world. The common goals of this community are the understanding of the fundamental physics of

these new systems and the exploitation of their novel properties. Since electronic and optical characteristics of QD are directly related to their size, shape, and composition, it is important to identify the microscopical processes that underlie the QD formation and evolution, as well as to understand how these processes are influenced by the growth parameters (such as temperature, flux, total coverage, etc). This demands careful and systematic atomic-level structural studies, such as provided by scanning tunneling microscopy (STM).

All the investigations reported in this dissertation are based on STM experiments performed on self-organized semiconductor QDs. In particular, we investigated the two most important model systems, InAs/GaAs(001) and Ge/Si(001). Our focus has been on the fundamentals of the QD growth and evolution (during annealing, etching and overgrowth experiments) and on developing an atomistic understanding of these phenomena. Most of the subjects addressed in the following pages are still a matter of intense research.

The thesis is structured as follows:

In chapter 2 a brief description of the experimental setup used through this work is given. The ultra-high-vacuum STM, its coupling to the III-V and Ge/Si molecular beam epitaxy growth systems, and various aspects of the sample growth and handling are described.

The exact shape and the atomic-scale features of InAs/GaAs(001) quantum dots grown close to thermodynamic equilibrium are elucidated and compared with theoretical models in chapter 3.

Chapter 4 is dedicated to studying the morphological transformations that InAs/GaAs island undergo during overgrowth. The experimental results are interpreted in terms of a delicate interplay between thermodynamic and kinetic effects.

The morphological transitions that occur during annealing experiments of Ge islands formed on Si(001) are the topics of chapter 5. A high-resolution analysis of this system reveals the detailed pathway followed by pyramid islands during their evolution towards multifaceted dome-like islands. Based on atomistic arguments derived from recent theoretical investigations, a simple model that captures the essential

features of this transformation is also presented.

A novel approach for the fabrication of nanostructures based on the formation of self-organized QDs in the SK mode, as well as the first results obtained with this method are described in chapter 6.

Chapter 2

Experimental setup

2.1 Introduction

Scanning Tunneling Microscopy is one of the most important experimental techniques used in the research field of nanometer-scale science. Since its invention in 1981 by G. Binnig, H. Rohrer, Ch. Gerber and E. Weibel, it has continuously broadened our perception about atomic scale structures and processes. Moreover the tip can be regarded as a powerful local probe providing a broad range of information about nanometer scale properties of matter which are often inaccessible by any other experimental technique [22]: electronic, vibrational and optical characteristics of nanostructures can be measured with sub-nm resolution and correlated to the local atomic and molecular morphology.

Molecular Beam epitaxy (MBE) is one of the most well established techniques for growing semiconductor heterostructures, its success is owed in great part to the capability to grow samples in a very precise and controlled way, since the fluxes of species delivered to the sample surface can be controlled with atomic precision (deposition rates in the range of ML/s are of common use). In that way, atomically thin layers, artificial superlattices and low dimensional quantum structures can be produced.

Although at present it is possible to find experimental arrangements where MBE and STM systems are coupled, these kind of equipments are rarely used as analysis
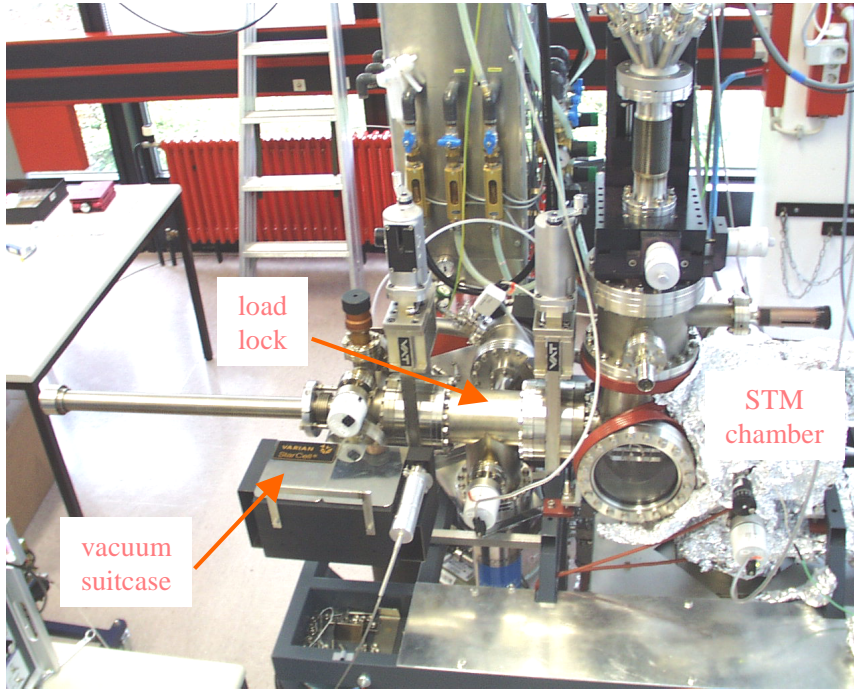
Figure 2.1: Experimental setup and its main parts: vacuum suitcase, load
lock and STM chamber.

tools in commercial processing facilities. In fact, most of the MBE-STM instru-
ments, commercial or home-built, are dedicated systems which permit to perform
experiments with just one specific family of compounds. Moreover the growth is typ-
ically done on a small piece of wafer inserted in custom-made sample holders and all
the evaporation cells, as well as the growth chamber itself, are designed in order to
fulfill such size constrains. The growth performed in these type of systems results in
samples whose quality (especially electronic) is lower than those grown by conven-
tional production-line MBE apparatuses, where full wafers are used. This is mainly
due to the large effusion cells of conventional MBE systems, that allow to grow thick
buffer layers in order to overcome the high defect density intrinsically present at the
pristine wafer surface. Moreover only in these large-scale growth apparatuses it be-
comes possible to produce multiple layers for contacts, mirrors, controlled doping,
etc. Therefore, if one wants to analyze exactly the same type of nanostructures that
are used for the realization of actual devices, the samples need to be produced in a
full-wafer MBE system. On the other hand, some of the large pumps that are used

for maintaining ultra high vacuum (UHV) in MBEs (in particular turbomolecular and cryogenic pumps) produce strong mechanical vibrations, absolutely incompatible with the stability requirements of STM.

Two solutions are therefore attainable, the first one being the realization of a combined apparatus in which the STM is permanently connected to a dedicated MBE. We decided to follow the second, less resource-consuming alternative of building an alone-standing STM, capable of hosting large wafer samples. A mobile, independently pumped UHV chamber (the so-called "UHV suitcase") is used in combination with two load-lock chambers, one at the MBE and the other at the STM, in order to transfer the samples from the growth to the analysis position under fully controlled UHV conditions. An important feature of this solution is the very rare opportunity of getting samples from two distinct MBE apparatuses (dedicated to the two main QD model systems, Ge/Si and InAs/GaAs respectively) and characterizing them in-situ with the same instrument.

2.2 MBE-STM

The experimental setup consists of three main parts: the STM chamber, the load lock chamber and the small UHV suitcase, see Fig. 2.1. In the following sections a general description of their main features will be provided. Further details on the design considerations followed for the construction of the STM chamber, the scanner-head, the damping system, the materials selection, etc., can be found in references [23, 24] where a very similar system is described. Nevertheless, an important difference distinguishes these two systems: in the apparatus developed by Leifeld *et al.* [23, 24] the whole STM chamber is used as a transfer system while, in our case, the STM remains immobile and a vacuum suitcase is used for transferring purposes.

2.2.1 STM chamber

The STM measurements are done in the chamber, where the STM head and the stage for loading and electrically contacting the samples are located. A base pressure in the
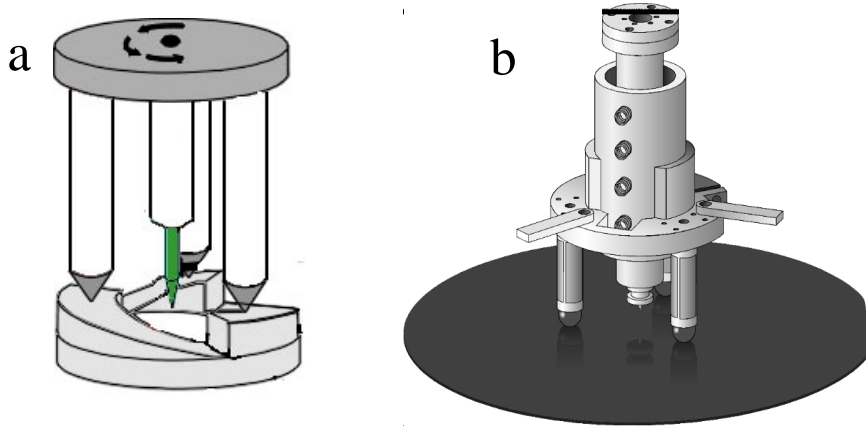
Figure 2.2: a) Sketch of the original "beetle" Besocke-STM [25]. b) STM-head design used in this work.

upper 10^{-11} mbar region is here sustained by means of a large ionic pump. The STM head is similar to the so-called "beetle" type, whose original design was proposed and developed by Besocke *et al.* [25]. The main difference of our STM head is that it lies directly on top of the wafer, see Fig. 2.2b, while the original beetle type is placed on three helical ramps, that are used for tip-sample approach, see Fig. 2.2a. In our configuration the coarse approach of the tip to the sample, is obtained by means of a linear motion motor (Burleigh Inchworm).

The most important feature of this design is the ability to probe a large area of the sample surface, up to 3.5 cm^2. The lateral movement on top of the wafer is achieved by means of three outer piezoelectric tubes (each terminating with a ruby ball) that support the STM head. Each piezoelectric tube is divided in four perpendicular segments that are independently contacted. By applying two inverted asymmetric sawtooth voltage signals to opposite segments of the three piezos, a linear or rotary stick-slip motion of the whole STM head is achieved. The ability of performing large lateral displacements is extremely useful for the characterization of samples where material is intentionally deposited in a non homogeneous way. Moreover, the special design of the STM head will be exploited for a future, already programmed, implementation of cross sectional STM measurements (XSTM). Small wafer samples containing capped QD structures will be broken inside the STM chamber and then positioned upright into appositely designed sample holders with the freshly broken
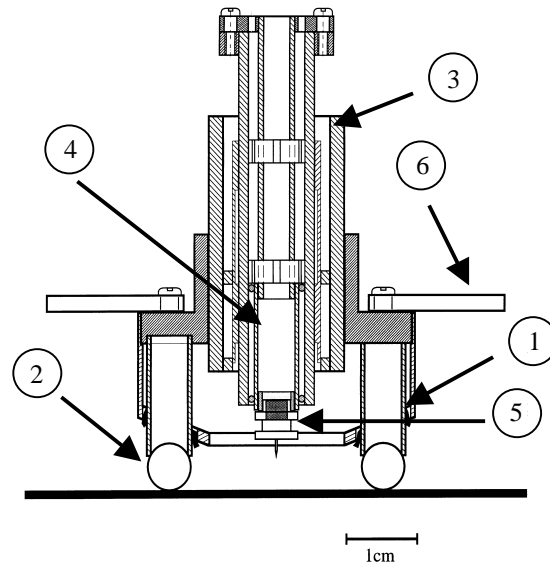
Figure 2.3: Scheme of the STM head: (1) outer piezo tube, (2) ruby ball, (3) inchworm, (4) scan piezo, (5) tip holder, (6) levers for lifting the STM head.

edge on top. The possibility of retracting the tip much farther than in usual STM designs (The inchworm motor has a travel length of several centimeters) will allow to approach and scan the surface of these special samples.

The cross sectional drawing in Fig. 2.3 shows the main parts of the STM head. Three identical piezoelectric tubes (1), each one with a ruby ball at the end (2), are glued to a holder containing the scanner and the coarse approach system. The Inchworm motor is mounted in the center of the scanner head (3) and inside its ceramic body the central piezoelectric tube is inserted (4). This provides the xy scan motion and the tip-sample distance signal needed for the feedback control. At its end a tip holder is placed (5) containing a CoSm magnet that allows tip exchanges with an *in-situ* tip dispenser (see later).

The STM head is surrounded by a sample stage that consists of two main parts (see Fig 2.4): a frame connected to the STM chamber chassis (1) and a heating-measurement stage (5). The former ends with 20 U-shaped silver pieces, each one lodging a CoSm magnet (2), while the latter has 16 corresponding copper pieces fixed at its top (3) and is suspended by four soft spiral springs (5). The magnets and copper blocks are intercalated and serve as an eddy current damping system when the sample stage is in the measurement position. For the purpose of providing isolation against
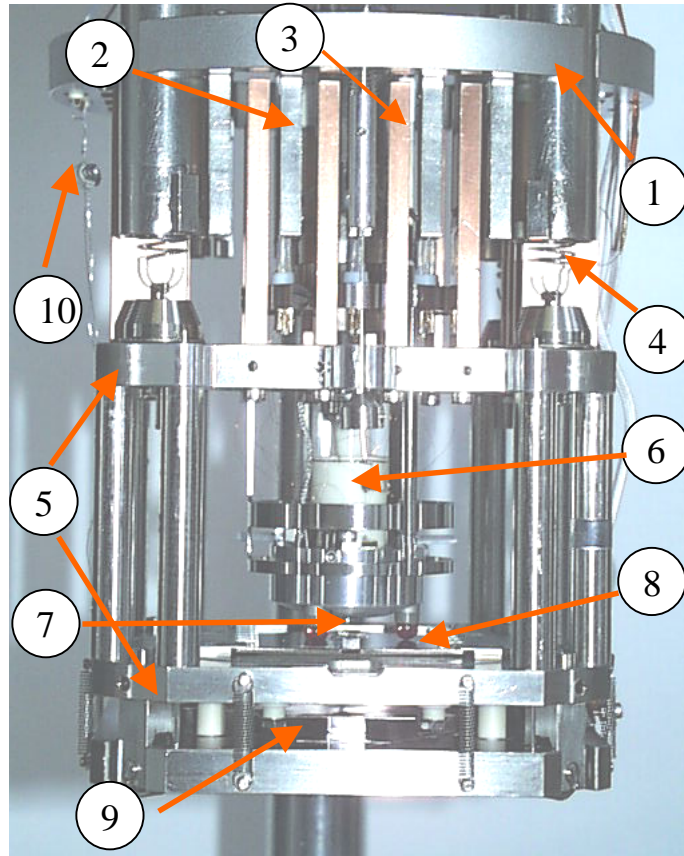
Figure 2.4: STM head inserted into the sample stage (measuring position). (1) Frame connected to STM chamber, (2) CoSm magnets, (3) Cu blocks, (4) springs, (5) heating-measurement stage, (6) STM head, (7) tip, (8) sample, (9) heater, (10) thermocouple wires.

mechanical and acoustical noise from outside, the STM and load lock chambers lie in a frame that is floating on laminar flow isolators. This assembly suppresses the coupling of low frequency vibrations during the measurements. [23, 24].

For STM measurements conducted on metallic substrates, the tip preparation is usually not a serious problem. Well-defined tips are easily obtained by a short, few Åmstrongs deep "dip" into the metal surface, since during the retraction a neck is formed and its breaking usually produces an atomically sharp "new" tip. Oppositely, on semiconductors surfaces the damage caused to the tip after crashing is most of the times irreversible. Therefore a mechanism for storing and replacing tips was implemented, that consists of a removable carrousel (carrying up to eight tips) and

of a transfer rod designed for holding the carrousel. Each time a new set of tips is needed, the transfer rod is attached to the load lock and the carrousel holding old or new tips is exchanged, without breaking the vacuum in the STM chamber. The possibility of tip exchange is particularly important when analyzing QD structures because convolution effects are more likely to influence the measurements of steep 3D clusters than those of samples containing shallow surface structures. As consequence the search for a proper tip can be quite tedious and pass through various unsuccessful attempts.

2.2.2   Load lock and Vacuum suitcase

The sample transfers between the MBE growth systems and the STM chamber are made by means of a small and independently pumped vacuum suitcase. An ionic pump is used to maintain the suitcase always under UHV conditions (base pressure $\sim 7\text{x}10^{-10}$ mbar) and a long cable is used to provide the electric power (MBE machines and STM equipment are located in two adjacent rooms). Nevertheless a battery could also be used, in order to get samples from farther located growth facilities. The whole vacuum suitcase is mounted on a trolley, as seen in Fig. 2.6d, which allows its transport from one laboratory to the other. A transfer rod on the chamber backside is used for the actual handling of the samples (see following section).

Before starting the growth of a new sample, the vacuum suitcase needs to be attached to the load lock of the MBE system and this is usually done the evening preceding the growth. In order to improve the pressure during the transfer between the MBE and the vacuum suitcase, both chambers are baked overnight. Once the growth is accomplished, the sample is moved into the vacuum suitcase and this is then transported to the neighboring lab, where it is connected to the STM load lock. Immediately after, the load lock is pumped down from atmospheric pressure to $\sim 1\text{x}10^{-9}$ mbar by using a combination of turbomolecular and cryogenic pumps. A 2 hrs. bake out (120°C) of the sole load-lock chamber is also performed. In the meantime, the gate valves to the STM and to the vacuum suitcase are wrapped with flexible water hoses in order to avoid any temperature (and consequently pressure)
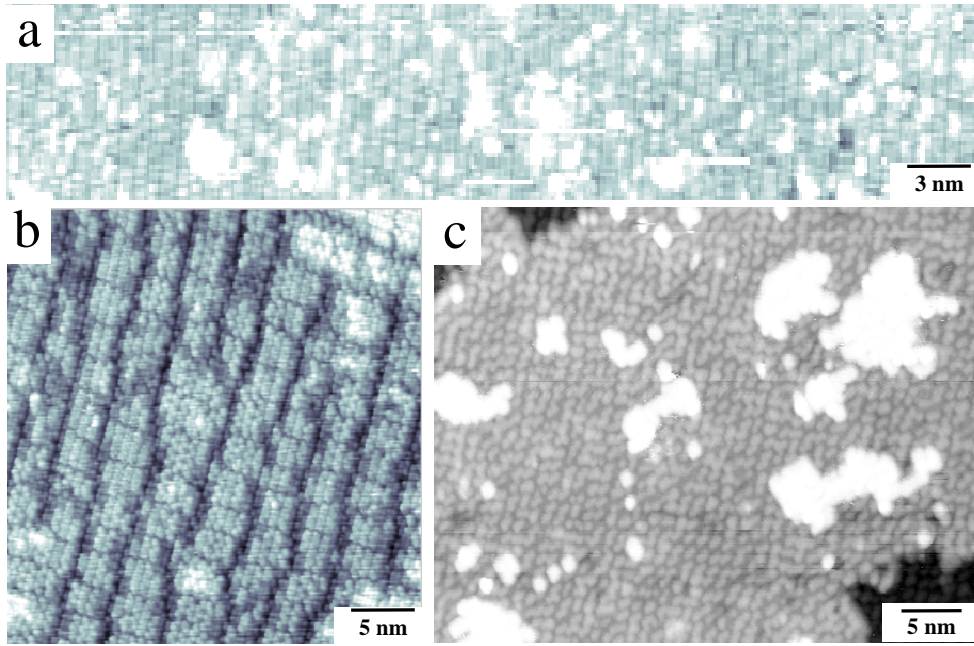
Figure 2.5: STM images of different surfaces exposed to the lowest vacuum attainable during the transfer procedure. a) Si(001) surface where extra dimers visible as bright bumps indicate that oxidation has occurred. b), c) clean surfaces of Ge/Si(001) and GaAs(001) samples respectively. The surface reconstructions can be clearly distinguished on both samples and no contamination effects are visible.

increase in these chambers. This procedure is aimed to enhance the pumping rate for getting the best trade-off between a short residence time of the sample in the vacuum suitcase and a low pressure during the following transfer to the measurement stage. When the desired pressure is reached, the sample is moved as fast as possible to the STM chamber and is placed in its measuring position. The completion of all these steps, comprising the sample growth, takes on average 24 hrs. The search of optimal conditions for performing the whole transfer procedure, implied a lot of initial try-and-error experiments. Nevertheless, we found that the average vacuum pressure attainable in each one of the load lock chambers ($\sim$ 1-3x10^{-9} mbar) is not low enough for handling pure Silicon samples. The effect of exposing a Si(001) substrate to these pressures can be observed in Fig 2.5a, where extra Si dimers, visible as bright bumps, are a characteristic indication that an oxidation reaction has ocurred [26]. Conversely,
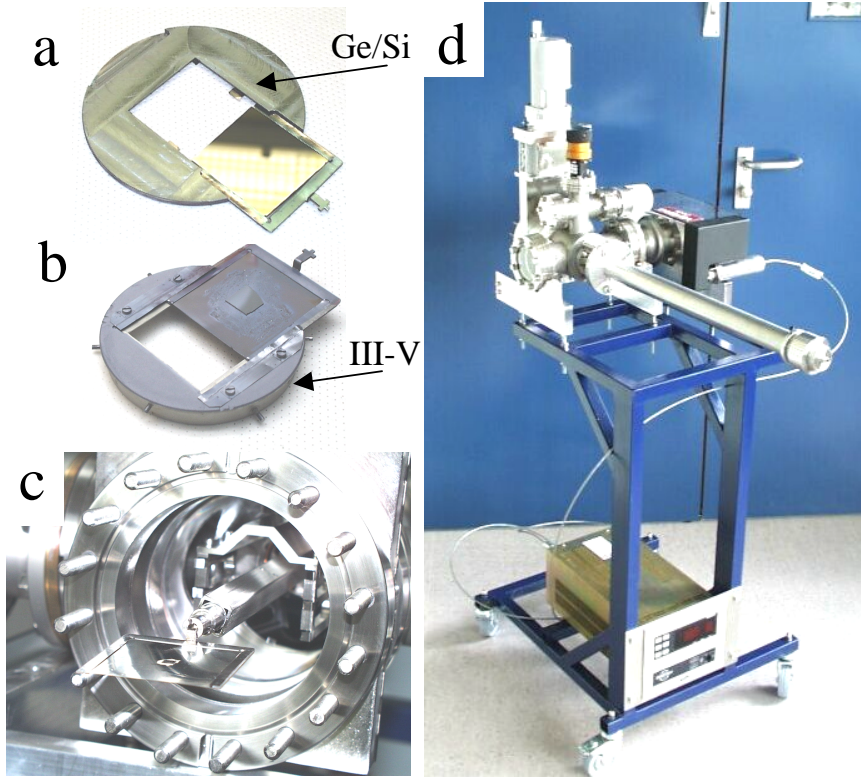
Figure 2.6: Images a) and b) show the modified wafer holders used in the Ge/Si and III-V MBE systems respectively. In both cases the forks used for holding the samples are also shown. c) Simulation of sample transfer done in air. Note how the transfer rod is holding the fork by means of a bayonet system. d) Vacuum suitcase mounted on the trolley. The transfer rod and the ionic pump, as well as the pump controller can be easily recognized.

in the case of Ge/Si(001) or III-V compounds, clean surfaces can be preserved without any contamination problem, as shown in Figs. 2.5b and 2.5c. This strong difference results from the high reactivity of the Si(001) surface, since the sticking coefficient of most contaminants (O_2, H_2O) is almost one [27, 28], whilst in the case of III-V surfaces and of Ge or Ge terminated ones, it is 10^3 times lower [29, 30, 31].

2.3 Sample Handling

All the measurements presented in this thesis have been performed on samples grown by conventional solid source molecular beam epitaxy in two different apparatuses,

which use wafers of GaAs(001) and Si(001) with a diameter of 2" and 3" respectively. A detailed description of the growth systems can be found in references [32] and [33]. The two MBE apparatuses require two different types of sample holders, while only one type of sample holder can be used in the STM. A solution compatible with the different geometrical constrains is obtained by fixing the basic sample size to a 5x5 cm^2 square (this size still allows the transfer trough 100 CF flanges), hosted in a fork-shaped sample holder, see Figs 2.6a and 2.6b. These metallic forks are made of tantalum and have a small "T"-like handle that fits the bayonet mechanism of the transfer rod in the vacuum suitcase. In this way they can be catched, moved and released during the transfer between the MBE and STM systems, as shown in Fig. 2.6c. While the forks fit directly into the STM heating-measurement stage (see Fig. 2.4), special 2" and 3" molybdenum "dummy" wafer holders are needed for the combination with the MBE systems. These extra holders are supplied with special grooves where the forks can be slid into (see Figs. 2.6a and 2.6b), obtaining in this way a good thermal coupling between sample and MBE heater. After the growth is finished, the forks are smoothly removed from the holders and transferred into the vacuum suitcase for successive transport. In case a Ge/Si sample is grown, the substrate consists of a 5x5 cm^2 piece of Si(001) wafer (Fig 2.6a), while for an InAs/GaAs sample, a small ($\sim$ 1.5x1.5 cm^2) piece of GaAs(001) wafer is glued with indium on a 5x5 cm^2 Si(001) support (Fig. 2.6b). This is because of the high prices of GaAs(001) substrates, $\sim$ \$100 US dollar per 2" unit. In order to avoid possible contamination problems, no exchange between forks used in the III-V and SiGe MBEs is ever done.

Chapter 3

InAs quantum dots

3.1 Introduction

Self-organized III-V QDs are nanostructures where important new ideas relevant to the basic physics of zero dimensional systems have been developed. Nevertheless, it is on the applications side that they have made their greatest impact, and this is particularly true for the InAs/GaAs(100) material combination. The potential advantages of using InAs QDs have been verified on actual devices, e.g lasers [35], high speed transistors, and uncooled infrared systems, including IR photodetecting imaging sensors [36]. It appeared for example, that the use of InAs QDs in diode lasers has several decisive technological advantages: (i) largely extended wavelength control by QD size and composition (lasing wavelengths could be achieved in the 1.3-1.5 μm spectral range, important for telecom and free-space applications) [5, 37]; (ii) very low threshold current densities at room temperature (~ 25 A/cm^2 per QD sheet) [5], and (iii) reduction of nonequilibrium carrier spreading and nonradiative recombination [38].

On the other hand, because of the statistical nature of growth, self-organized dots are usually not very uniform in size, posing severe limits for device applications. In fact, width, height and shape of QDs influence the quantum confinement of charge carriers and determine their optoelectronic properties. As a consequence, the size fluctuations of a typical dot ensemble cause a large and undesired spread in its elec-

tronic and optical properties. A precise control over the morphological parameters of QDs is therefore of crucial importance, but at present, still difficult to obtain. This is testified by the number of different and sometimes contradictory experimental results that have been reported in literature for InAs/GaAs(001): widths ranging from 10 nm to 40 nm, heights from 2 to 10 nm and shapes such as lenses, truncated pyramids and a variety of multi-facetted structures [39, 40, 41, 42]. Turning to theory, very few is known and most of the proposed models base on thermodynamic equilibrium hypotheses. These allow to consider only ensemble-averaged parameters neglecting complex kinetic aspects that are difficult to treat for semiconductor systems. Apart from the possibility of a direct comparison with theoretical predictions, the growth of semiconductor QDs under thermodynamic equilibrium would be extremely favorable for device-oriented applications too. In fact, thermodynamic equilibrium conditions are much more stable and less sensitive to small variations in the experimental parameters and thus allow a higher degree of reproducibility and transferability of the achieved results.

In order to approach the regime where thermodynamic equilibrium conditions are relevant and to minimize the importance of kinetic effects, the QDs investigated in this chapter were grown at high temperatures and extremely low growth rates. A further positive effect of this choice is the production of "large" QDs characterized by light emission wavelengths close to the technologically relevant 1.3 μm [43] and with linewidths as narrow as 16 meV [44]. These QDs are analyzed by means of in-situ STM measurements, whose ultimate resolution allows to perform a systematic atomic-level structural study.

## 3.2 InAs/GaAs(100) quantum dots close to thermodynamic equilibrium

We used semi-insulating GaAs(001) wafers as substrates and removed their natural oxide by 10 min heating at 640°C in ultra high vacuum. A 400 nm GaAs buffer was deposited thereafter by MBE at a flux of 0.6 monolayers per second (ML/s), holding
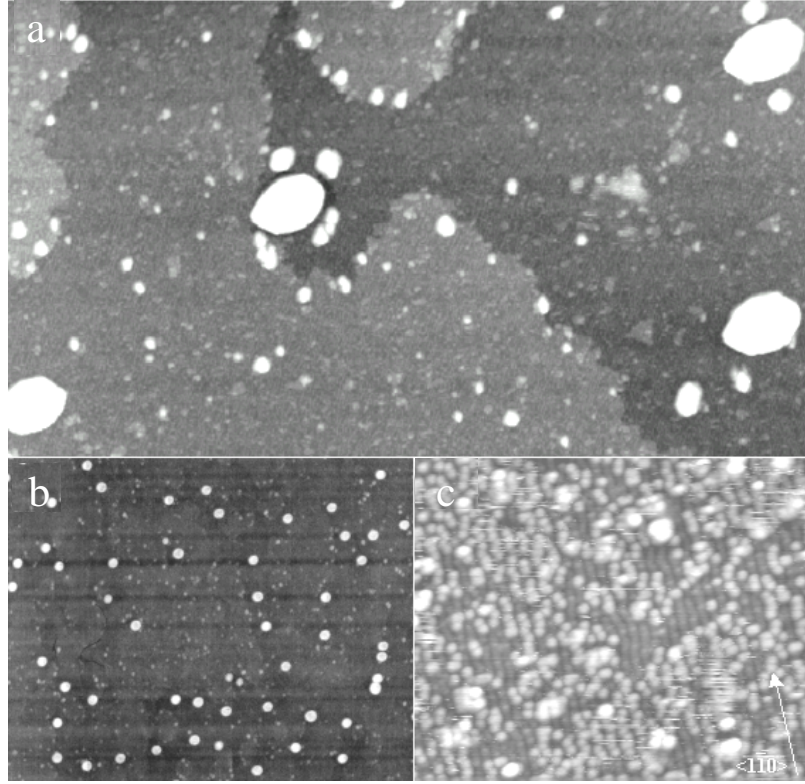
Figure 3.1: (a) 500x280 nm^2 STM image of 1.8 ML InAs on GaAs(001). The image contrast has been enhanced to show surface details. (b) 2.0x1.6 μm^2 ex-situ AFM scan of the same sample. (c) High resolution STM image of the wetting layer showing (2x4) (light gray) and (1x3) (dark gray) reconstructed domains.

the substrate at 610°C. Flux calibration was done by means of reflection high energy electron diffraction (RHEED) intensity oscillations, while the RHEED monitoring of the (2x4) → c(4x4) transition in the surface reconstruction was used for calibrating the sample temperature at 500°C. The actual QDs were grown by deposition of 1.8 ML of InAs at 0.008 ML/s with the substrate at 500°C and an As pressure of 8x10^{-6} mbar. Immediately after closing the In shutter, the substrate heater was turned off while keeping a constant As pressure, resulting in an initial cooling rate of 1°C/s. As soon as room temperature was reached, the samples were transferred under UHV conditions to the STM chamber, where STM images were taken in the constant current mode with typical tunneling currents of 0.1 nA and voltage biases of -3.0 V

(filled states).
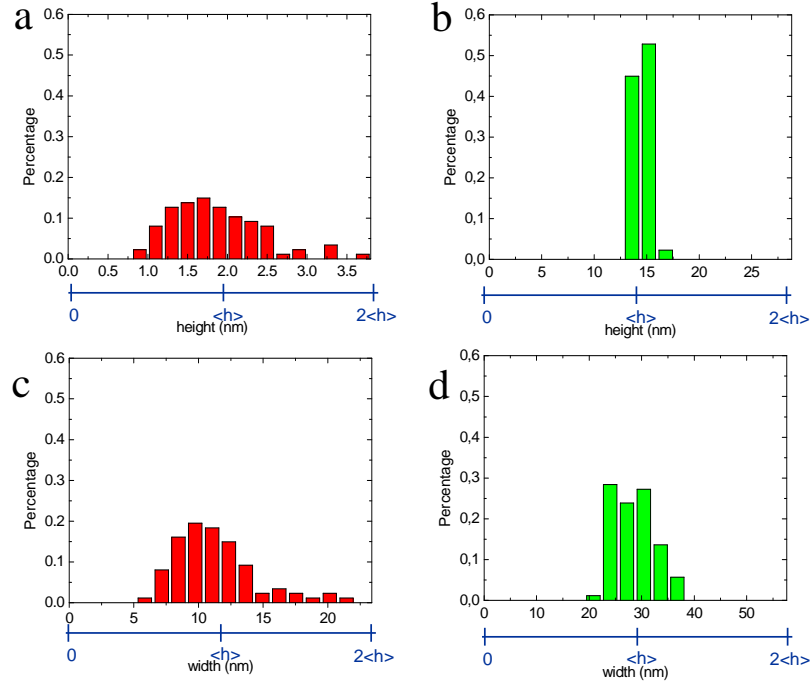
Figure 3.2: Histograms showing the normalized width and height distributions for small (a) and (c), and large dots (b) and (d). Note the extremely narrow distribution ($< 5\%$) in the height of the large dots.

Figure 3.1a shows a characteristic STM surface topography after the deposition of 1.8 ML InAs on GaAs(001). Two types of QDs are clearly recognizable: "small" and "large" dots with surface densities of $7\text{x}10^{10}\ cm^{-2}$ and $3\text{x}10^{9}\ cm^{-2}$ respectively, that were determined by analyzing a large number of wide-area atomic force microscopy (AFM) scans similar to that shown in Fig. 3.1b. The structure of the wetting layer (WL) could be determined by means of high resolution STM images, see Fig. 3.1c, and manifests the coexistence of two surface reconstructions, the (2x4) and the (1x3), in agreement with the observations in [45]. More details about the wetting layer structure will be given in Appendix A. A bimodal size distribution of QDs in the InAs/GaAs(001) system has already been reported by F. Patella *et al.* [46], but in that case the small dots had a narrower size distribution and the larger were, most probably, the result of a ripening process. Conversely, our measurements indicate that the large QDs (see Figs. 3.2a and 3.2b) have an extremely narrow size distribution
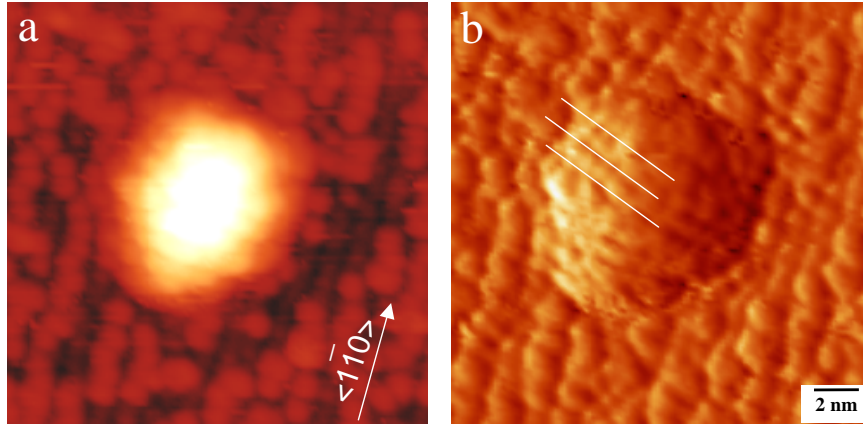
Figure 3.3: a) STM image of a "small" QD. b) Horizontal derivative of the same image. This treatment enhances small scale details and reveals atomic features of the QD facets that are similar to those reported by Márquez *et al.* [39].

(standard deviations of 5% for the height and 10% for the lateral dimension) while the smaller ones show large relative variations in height and width (see Figs. 3.2c and 3.2d). This fits much better with the results reported in refs [47, 48].

Even if most of the small QDs do not have any well-defined shape and might be interpreted as precursors of fully developed QDs, a smaller fraction is composed by facetted islands (see Fig. 3.3) with an irregular hexagonal base slightly elongated along $< 1\bar{1}0 >$. These are typically 14 ± 3 nm wide and 2.4 ± 0.5 nm high, and a measurement of the angles between their facets and the (001) plane allows an assignment to the (137) orientation, in accordance with the reported in [39]. Recently Kiravittaya *et al.* [49] demonstrated that a 30 sec. growth interruption after the InAs deposition is sufficient for the complete disappearance of the small dots, while the larger ones remain almost unchanged. This is a first indication that while the large QDs are thermodynamic stable structures, small ones are only metastable and most probably correspond to local and not global thermodynamic minima.

High resolution STM images as Fig. 3.4a show that the large dots have the shape of an octagonal based pyramid and are slightly elongated perpendicularly to the WL dimer lines (i.e. along $< 110 >$). Their typical widths are 25 ± 4 nm
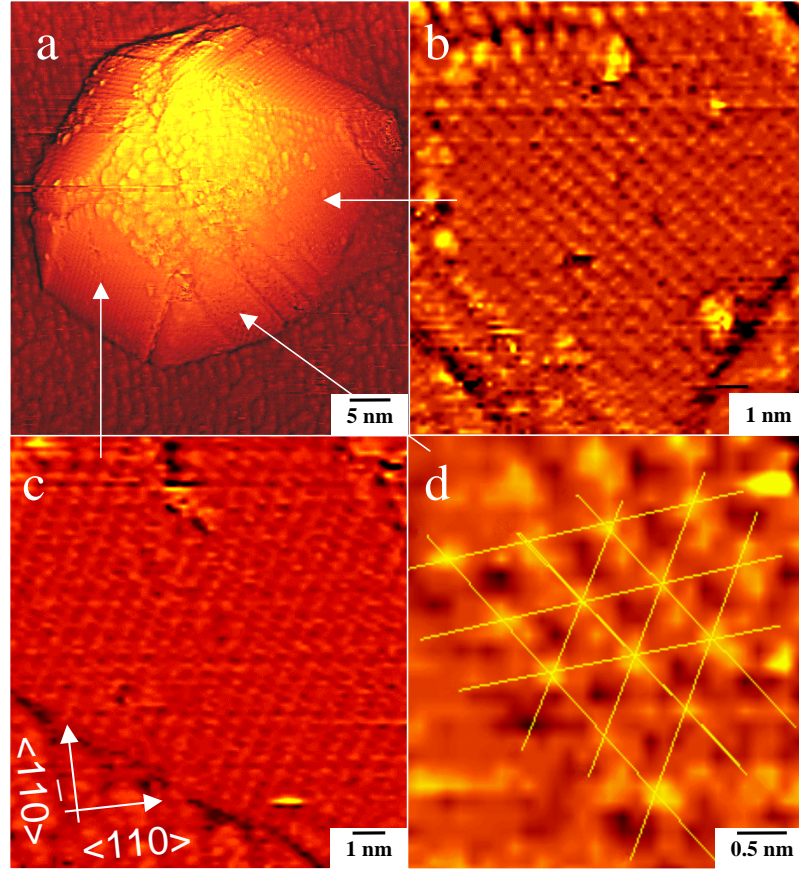
Figure 3.4: (a) STM topography of a large island. (b) and (c), high-resolution views of two (011) facets, that show a (1x1) surface reconstruction with rectangular symmetry. (d) High-resolution image of a (111) facet of the same island. Lines have been superimposed for better visualizing the triangular symmetry of the (2x2) reconstruction.

along $< 1\bar{1}0 >$ and 44 ± 4 nm along $< 110 >$ and their height is 14.4 ± 0.7 nm. Despite these large dimensions, the dots are dislocation-free, as confirmed by good photoluminescence properties and transmission electron microscopy measurements [50]. A closer inspection of STM topographs reveals that the sides of these QDs are composed of only two type of facets, namely (011) and (111). This is revealed by imaging the facets with atomic resolution, see Figs. 3.4b-d. Such measurements are much more reliable than the sole determination of facet angles and show a rectangular lattice for the (011) planes, Figs. 3.4b and 3.4c, and a triangular one for the (111) planes, see Fig. 3.4d. Moreover, the evaluation of the lattice parameters (calibrated
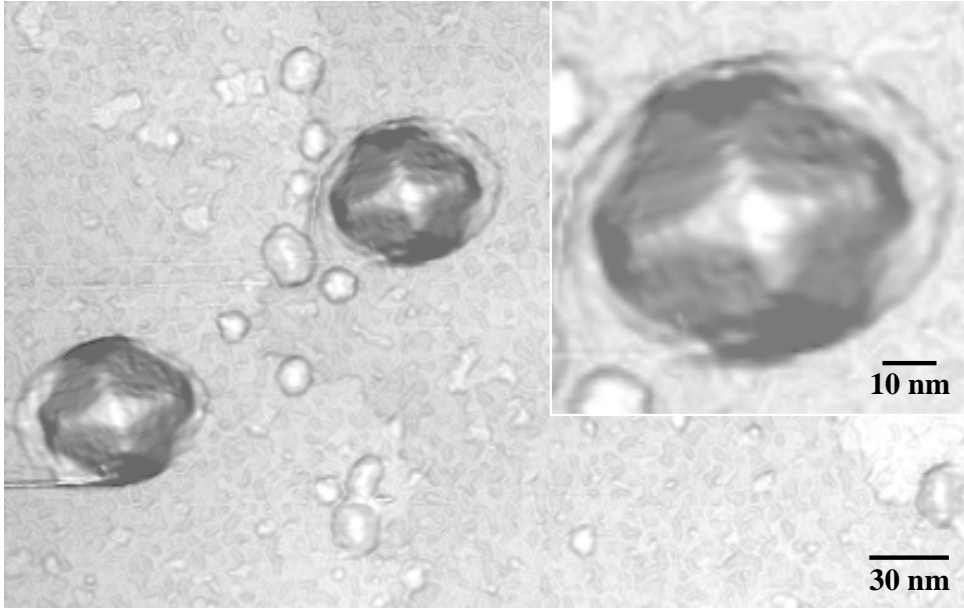
Figure 3.5: STM image of coexisting small and large InAs/GaAs(001) islands. The gray scale corresponds to the modulus of the local surface gradient. Contrarily to Fig. 3.4, the dot top is clearly recognizable as being formed by shallow triangular facets. Moreover, shallow facets can be observed also at the base of the large dots. The inset shows a magnification of a large QD.

in respect to the WL reconstruction in the same image) allows the identification of the surface reconstructions which turn out to be (1x1) for (011) and (2x2) for (111).

As evidenced by the high resolution STM image in Figure 3.4a, the top of the island can not be clearly visualized, most probably because of the convolution between a not well-defined part of the tip and the islands. Note that since the large dots are very steep (angles of 40°-60°), it is fully plausible that during scanning different parts of the tip tunnel with different parts of the islands. In order to determine the exact shape of the free standing QDs, we turn to lower resolution measurements that are free from tip artifacts. A representative STM topography is shown in Fig. 3.5, where, in order to enhance the contrast between areas with different slopes, a gray scale corresponding to the modulus of the local surface gradient is used.

The (011) and (111) facets already identified in the high resolution images are here represented by lighter and darker areas respectively. In addition, shallower facets are

clearly imaged as even lighter regions at the dot foot, as well as small triangular regions at the dot top (see inset of Fig. 3.5). In order to get quantitative values for the facet orientations also from these lower-resolution data, we refer to the so-called facet plot (FP) analysis. This corresponds to plot the local surface gradient in a two-dimensional histogram so that all the points of a STM image that have a given surface orientation contribute to the same spot in the FP (more details can be found in refs. [51, 52]). Fig. 3.6b shows the application of this method to the large dots: besides the spots corresponding to the already identified (011) and (111) facets, four further spots compatible with the (137) orientation are observed. These spots stem from the shallow facets that are observed both on the top and at the foot of the dots (see inset of Fig. 3.5). By doing the same analysis on small dots, only the central spots corresponding to the (137) are visible, see Fig. 3.6a. This confirms our previous assignation and the results published by Màrquez *et al.* [39] but explicitly excludes other facet orientation proposed in literature for shallow InAs/GaAs(001) QDs: (113),(215), etc. [41, 53]. All these experimental results are summarized in the structural models of Fig. 3.6c that we propose for small and large InAs islands grown on GaAs(001).

The accurate experimental determination of the shape of large QDs allows a meaningful comparison with recent theoretical predictions for the equilibrium shape (ES) of coherently strained (i.e. dislocation-free) InAs islands grown on GaAs(001) [55, 56, 57]. M. Scheffler and collaborators have developed an hybrid approach in which the surface reconstructions, the surface energies and their strain dependence are calculated *ab-initio* by density functional theory (DFT), while the long-range strain relaxation in the QDs and in the underlying substrate are determined by continuum elasticity theory applying a finite-element approach. The good agreement between these theoretically predicted ES and our experimental findings for large InAs/GaAs(001) QDs is demonstrated by the comparison between Figs. 3.6c and 3.7a. This agreement extends also to the surface reconstructions of the island facets, since DFT calculations predict that the energetically preferred reconstructions are a relaxed (1x1) cleavage plane for InAs(011) and two different (2x2) reconstructions
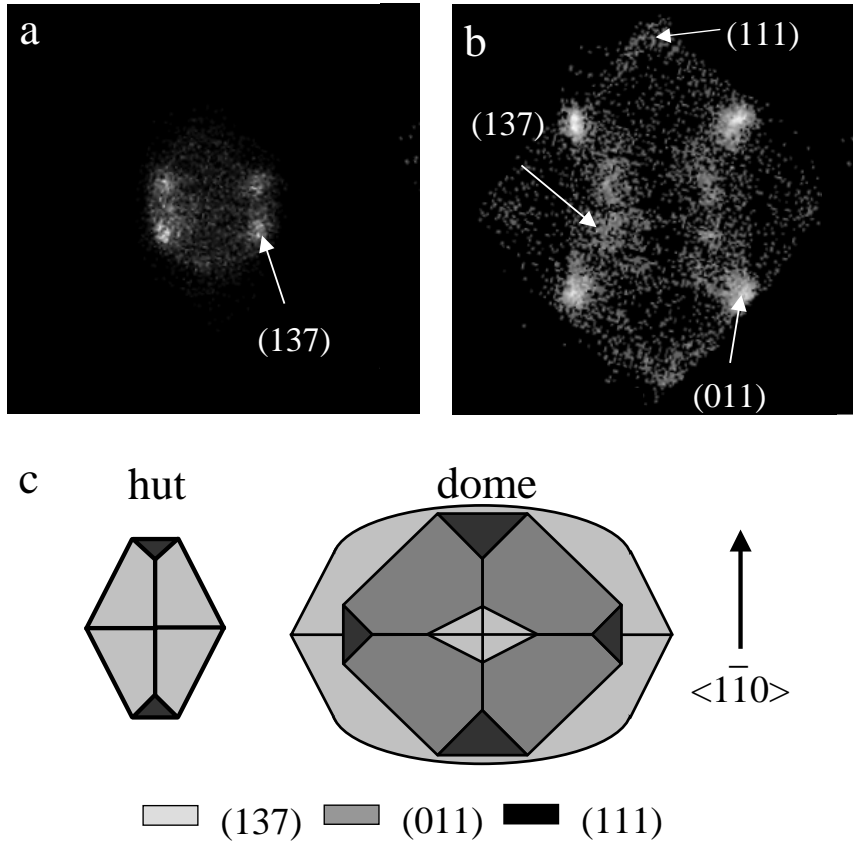
Figure 3.6: a) Facet plots corresponding to coexisting (a) small and (b) large InAs/GaAs(001) QDs. The facet orientations corresponding to the principal spots are explicitly indicated. c) Structural models of the two type of islands. The different facets are identified through the reported greyscale code. The presence of small (111) facets in the InAs pyramids is inferred from the STM images but is not directly observable in the facet plots, because of the low intensity of the corresponding spots. The same is true for the small ($\bar{1}37$) facets in InAs domes, whose presence is deduced from their intersection with the (011) facets.

for InAs(111) and InAs($\bar{1}\bar{1}\bar{1}$) [56], see fig. 3.7b (for the experimental data, see the atomic resolution images in Figs. 3.4b-d). The theoretical calculation of the ES does not predict the shallow (137) facets experimentally seen at the top and the foot of the islands. This is because only low-index surfaces were considered in the total energy minimization algorithm, with the consequence that the (probably) lower-energy
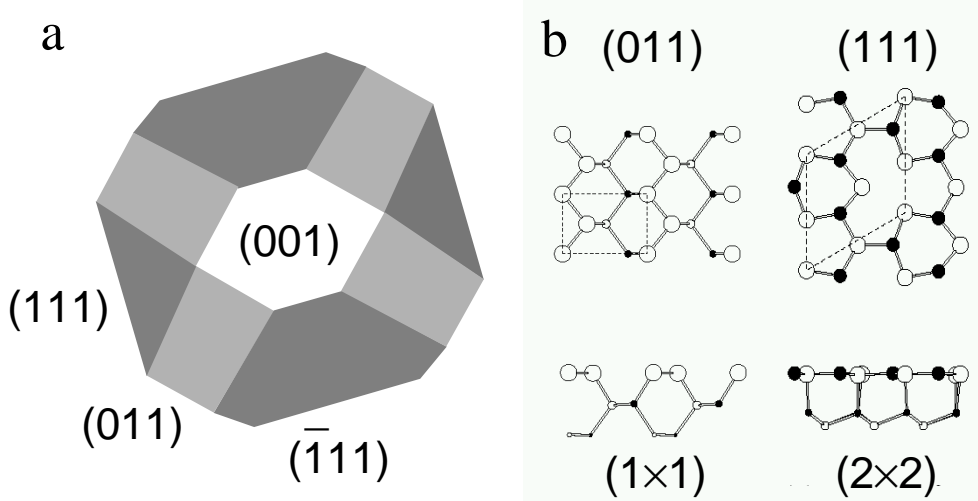
Figure 3.7: a) Equilibrium shape predicted for an InAs/GaAs(001) Quantum dot in thermodynamic equilibrium (ref. [54]). b) Atomic structure models for the (011) and (111) InAs surfaces with the most energetically favorable surface reconstructions.

(137) orientation was artificially substituted by the (001) one. More accurate simulations have been programmed in order to overcome this discrepancy [58]. Also the theoretically predicted values for the QD volume do not perfectly agree with the experimental ones, being a factor of 15 smaller than the actually measured value of $5x10^6 \mathring{A}^3$. The reason for this is most probably the strong dependence of the ES on the lattice mismatch [79], so that even small deviations from the theoretical value of 7.1% (due to Ga incorporation in the growing QD) can result in strong variations of the volume. A final difference is given by the ratio between the extensions of (011) and (111) facets that is experimentally larger than what predicted by theory. Apart from an experimentally smaller As partial pressure, this could also originate from residual kinetic effects, as for example the higher growing rate of (111) facets in respect to (011) ones [60]. Nevertheless, the agreement with the theory developed by Scheffler and coworkers, is overall very good and since that theory essentially relies on the hypothesis of thermodynamic equilibrium, this agreement represents a test on how close the chosen experimental parameters are to the thermodynamic equilibrium. The fact that we observe a bimodal size distribution is not compatible with this statement. In

fact the small islands can be considered as metastable equilibrium minima that disappear with an increased amount of deposited material or by means of a post-growth annealing [49]. Such an interpretation is supported by preliminary theoretical studies [58]. Finally, we notice that the results presented here are compatible with what has been reported in literature. Recently Murray *et al.* [42, 61] obtained quantum dot structures that were grown at comparably low rates and presented room temperature emission at 1.3 μm. The low resolution of their *ex-situ* AFM characterization does not allow any direct comparison, but sizes and densities of the QDs are comparable with our results. The presence of (011) and (111) orientations in multifaceted islands has also been derived from X-ray scattering measurements [62], even if the QDs were reported to be considerably smaller that what we actually measure. Apart from a difference in the deposition temperature and therefore in the QD composition, this could also be due to the difficulty of indirectly inferring heights and sizes of QDs from the width of broad crystal truncation rods [62]. The largest part of the literature concerned with InAs/GaAs(001) QDs concentrated on small dots (lateral dimensions < 20 nm, heights < 5 nm) for which a number of structural models has been proposed. Limiting only to the high resolution measurements (both in real [39, 41, 57] and in reciprocal space [53]), an agreement can be found on a facetted island shape with elongated hexagonal base and (137) main facets, according to the nice work of Márquez *et al.* [39].

Chapter 4

Overgrowth experiments

4.1 Introduction

A precise determination of the dimension and shape of QDs is of great importance since these morphological characteristics influence the quantum confinement of charge carriers and therefore define the QD opto-electronic properties. In the previous chapter we made a first step in determining these characteristics for the InAs/GaAs(001) system. However, the analysis of free-standing QDs alone is not sufficient, since strong morphological or compositional changes can take place during the capping of the islands with a larger band-gap material. This is an essential process for fabricating any devisable application and plays also an important role in the growth of multiple stacked layers of QDs, the so-called quantum dot superlattices, that are characterized by vertically aligned QDs, improved island uniformity and high spatial density [63, 64, 65, 66]. Recently, it was also shown that a combination of overgrowth, etching and regrowth processes can lead to the formation of laterally coupled QD molecules [67].

The possibility that the islands could remain structurally unchanged during overgrowth was discarded almost since research on semiconductor QDs started, with the first experiments on island capping [68, 69]. Since then several studies conducted on the InAs/GaAs system have attempted to explain the mechanisms underlying such changes, but at present a clear and conclusive description explaining that phenomenon

29

is still missing. Conversely, for the Ge/Si(001) system, overgrowth experiments done by Rastelli *et al.* [70] have clearly identified the different shape transitions suffered by the dot during the embedding, as well as the fundamental processes inducing those transformations.

Therefore, motivated by the lack of conclusive arguments explaining the overgrowth of InAs dots and by the importance that this process has in the development of QD-based devices, we decided to investigate the capping of InAs/GaAs(001) islands by means of in-situ scanning tunneling microscopy and to use its ultimate spatial resolution in order to identify the basic processes that are responsible for the morphological changes.

4.2   Morphological evolution during overgrowth

All the overgrowth experiments were conducted on QD samples obtained after depositing ~ 1.8 ML of InAs on GaAs(001) substrates by molecular beam epitaxy at an extremely low rate (0.008 ML/s) and high substrate temperature (500°C). As it has been shown in chapter 3, under these conditions the formation of InAs QDs close to thermodynamic equilibrium takes place. Although smaller dots (height ~ 2 nm) are also formed, the present investigation is mainly focused on the capping of large islands (~ 14 nm). The overgrowth experiments were done by depositing increasing amounts of GaAs ranging form 1 up to 11 ML, while keeping a substrate temperature of 460°C in order to avoid Indium desorption and to reduce intermixing effects. Different deposition fluxes (0.08 and 0.6 ML/s) were used in order to change the time scale and therefore to elucidate the possible influence of kinetic effects on the capping process.

Fig. 4.1 shows the morphological evolution that occurs during overgrowth, when dosing GaAs at the lowest flux (0.8 ML/s). Even at the very first stages of capping (1 ML) the comparison between Figs. 4.1a and 4.1b shows that crucial changes take place: material starts to arrange in the surroundings of the dots and the dots height is considerably reduced (see later). After depositing 3 ML of GaAs, the shape of the
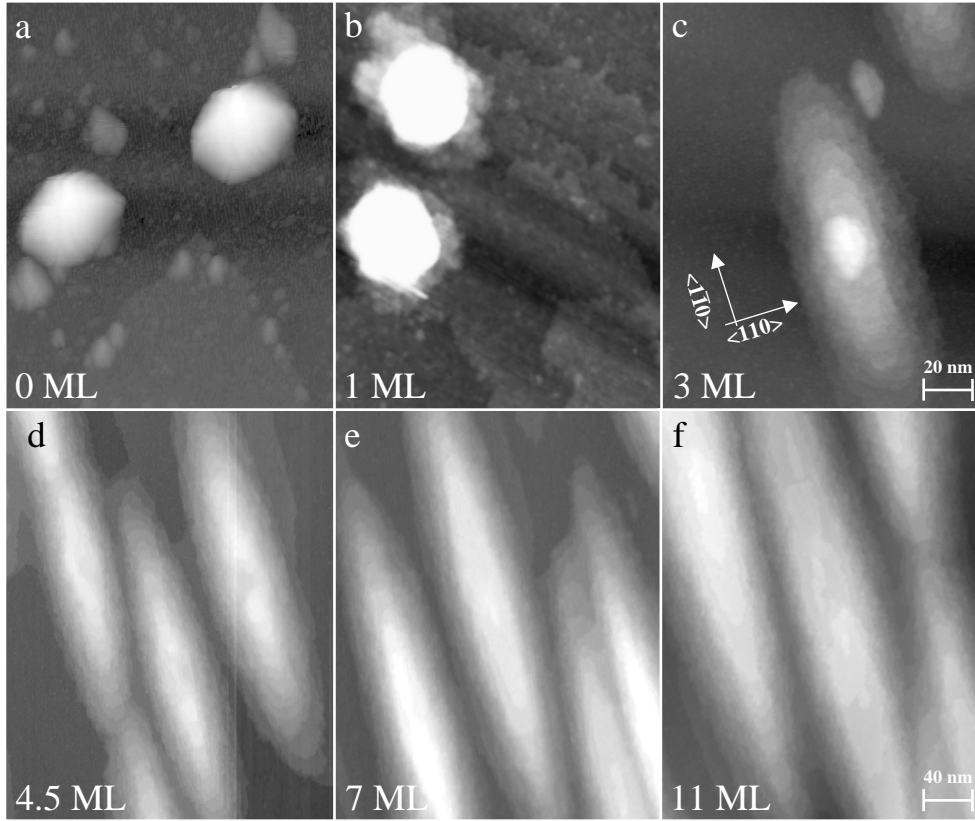
Figure 4.1: Representative STM images showing the morphological evolution undergone by InAs QDs during overgrowth experiments. The images correspond to different amounts of GaAs (0-11 ML) deposited at a flux of 0.08 ML/s. Gray scales correspond to the local height, but have been adjusted independently for each image in order to enhance the morphological details.

island is drastically modified: the QDs have transformed in elongated structures with a major axis parallel to $< 1\bar{1}0 >$, and only a small part of the original dot is still protruding at their center (Fig. 4.1c). As more GaAs is deposited (4-11 ML), the original dot disappear completely, while the elongated structures continue increasing their length and width, until they meet each and form a sort of ripples that cover the entire surface (Figs. 4.1d-4.1f).

In order to get quantitative data, STM linescans of the dots were taken for the different stages of capping. Figure 4.2a displays representative scan profiles along the $< 1\bar{1}0 >$ direction that have been shifted vertically with respect to the wetting layer
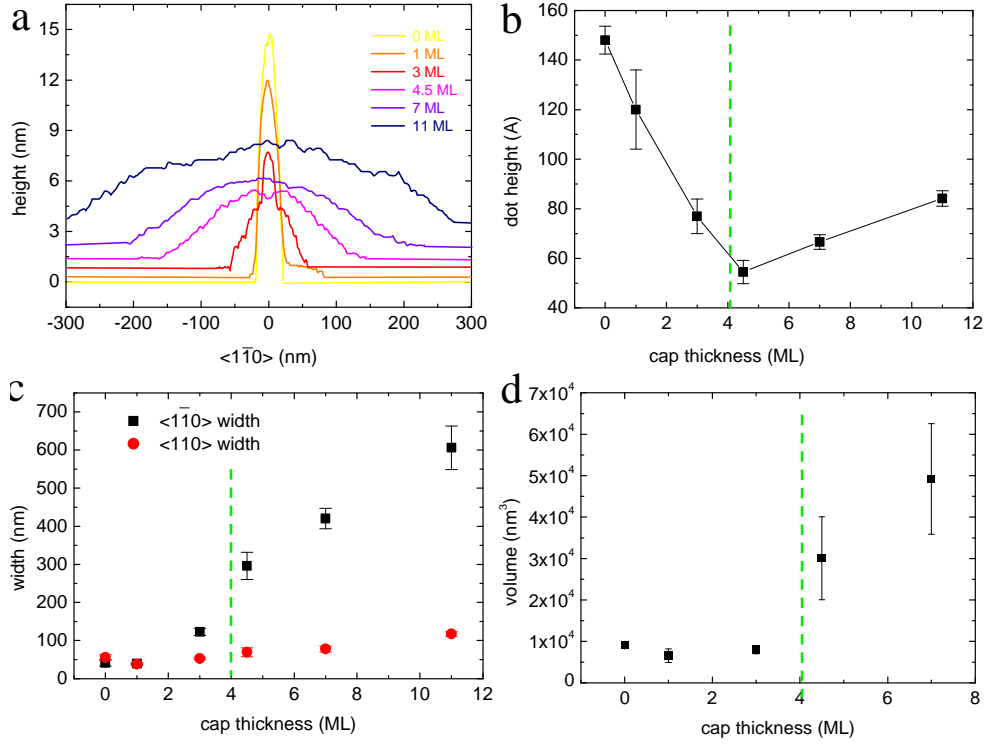
Figure 4.2: a) Representative STM scan profiles along $< 1\bar{1}0 >$ for the different stages of QD overgrowth. (b-d) Evolution of the height (b), width (c) and volume (d) as a function of the capping thickness. The existence of two different time regimes can be recognized for each of these morphological parameters with a transition occurring at ~ 4.0 ML (vertical dashed line).

by the amount of nominally deposited GaAs. For example, the scan profile corresponding to 3 ML overgrowth (red line) has been shifted 0.85 nm with respect to the wetting layer of the as-grown dot (yellow line). By analyzing a large statistics of such linescans, average values for the QD height, width and volume were computed as a function of the cap thickness (Figs. 4.2b-d). Each morphological parameter shows the existence of two different capping regimes characterized by clearly different trends can be identified from the trends. For example, the evolution of the QD height in Fig. 4.2b shows that the overgrowth is characterized by an initial rapid dissolution of the QDs (in which the height decays linearly with the amount of deposited GaAs) followed by a slower real capping of the remaining structures (identified by a positive height vs. cap thickness slope). The transition from one regime to the other

takes place at certain "critical thickness" that, for the deposition parameters used in these experiments, corresponds to $\sim$ 4.0 ML. In the following we will discuss separately each regime and identify the microscopic processes that generate the respective morphological transformations.

4.2.1   First regime: Height decay of the dot

The strongest structural changes take place within the first few monolayers of deposited GaAs (Figs. 4.1a-c), and are accompanied by a height decay of $\sim$ 60% (Fig. 4.2b). In order to understand better these modifications and to determine whether they are linked, we refer to high resolution STM images of the overgrown dots. In Figures 4.3a-c, representative STM topographs of the different shapes acquired by the dots after been capped with GaAs (0-3 ML), are showed. In the 1 and 3 ML case, the images correspond to a zoom in the central part of the actual structure (compare with Figs. 4.1b and 4.1c). The corresponding facet plots with the indication of the main surface orientations are displayed in Figs. 4.3d-f.

Figure 4.3a corresponds to an uncapped dot, whose FP shows the laterally bounding (011) and (111) facets as well as the four small and shallow (137) facets on the dot apex (Fig. 4.3d). When these pristine dots are capped with 1 ML of GaAs, the (137) facets increase their size, extending almost down to the bottom of the islands (see Fig 4.3b), while the other facets drastically reduce their dimensions. That facet redistribution can be followed in Fig. 4.3e, with an evident increase in the intensities of the (137) spots and a corresponding attenuation of the (011) and (111) spots. As further material is deposited (3 ML), the remaining part of the dot transforms into a $< 1\bar{1}0 >$ elongated structure (see fig. 4.3c) characterized by a (001) top facet and four small lateral (137) facets. These can not be clearly distinguished from the STM image but appear as faint spots in the corresponding facet plot of Fig. 4.3f. Conversely the large (001) facet is revealed by the intense spot appearing at the center of the FP, that corresponds to the points on the surface having "zero slope". The bright line in the left part of Fig. 4.3f is an artifact that derives from an excessively fast scan rate used during the image acquisition, which hindered the adequate response
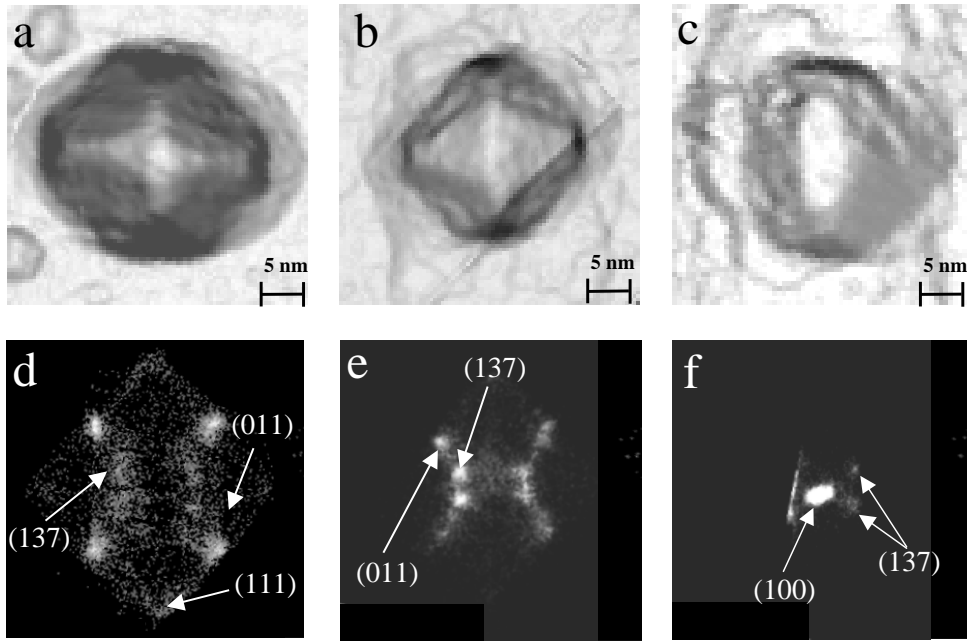
Figure 4.3: a)-c) STM images showing the shape transformation undergone by InAs QDs after the overgrowth with 0-3 ML of GaAs. The gray scale is given by the absolute value of the local surface gradient. d)-f) Corresponding facet plots showing the orientation of the main facets that compose the QD structures.

of the feedback loop.

Concerning the decrease of the dot height that takes place contemporary to the above shape transformations (we measure a reduction rate of ~ 2 nm/deposited ML), we notice that its correlation with the amount of deposited Ga atoms is confirmed by independent experiments done by Songmuang *et al* [67]. These authors covered similar InAs QDs with an $In_xGa_{1-x}As$ alloy (x=0.1-0.15) and observed that the rate of the dot height reduction scaled with the actual rate of Ga atoms arriving at the dot surface. Furthermore they also reported that, when the Ga content in the capping alloy is reduced to 80%, the dot is almost not dissolved and instead a true covering process is observed.

From these results, it clearly appears that the Ga atoms represent the key factor inducing the dot dissolution. The reason for this can be found in the surface segregation of group III elements. That is a well-known effect, taking place during the
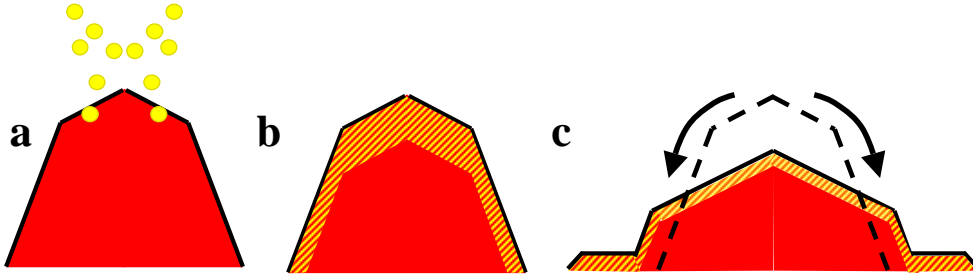
Figure 4.4: Schematic representation of the processes happening during the first stages of the QD overgrowth. a) Ga atoms arrive to the island, b) local intermixing occurs due to In segregation and Ga penetration beneath the surface, c) the shallower facets become larger by a material transport from the island top to its bottom.

growth of III-V heterostructures under certain growth conditions, in which is found a surface enrichment of one of the third-column components and is defined like the exchange reaction of atoms between only two atomic layers, the surface layer on top of the specimen and the bulk layer beneath [71]. In the case of InAs(001) surfaces overgrown by GaAs, it has been demonstrated that the probability of In-Ga exchange is very height at the substrate temperature that we used during the overgrowth experiments (460°C) [72]. We have independently confirmed that such exchange processes take place also for the samples analyzed in this chapter, by studying the segregation of Indium in flat surface regions far away from QD structures. The results of these investigations and the corresponding interpretation are discussed in the appendix A.

If In segregation happens while depositing GaAs on the pristine WL (for which the In/Ga ratio is around 25% [73]) the same process will for sure take place also on the QDs surface, where the In/Ga ratio approaches unity. In other words, during the capping process a certain fraction of In atoms segregates to the dot surface while the exchanged Ga atoms penetrate the subsurface layers. The net result is therefore a Ga incorporation that locally changes the average composition of the dot and consequently its strain status. This is the real origin of all the observed morphological transformations since the dot reacts to the decrease of the strain by reducing the extension of steep facets (that are more efficient in releasing strain but have a higher
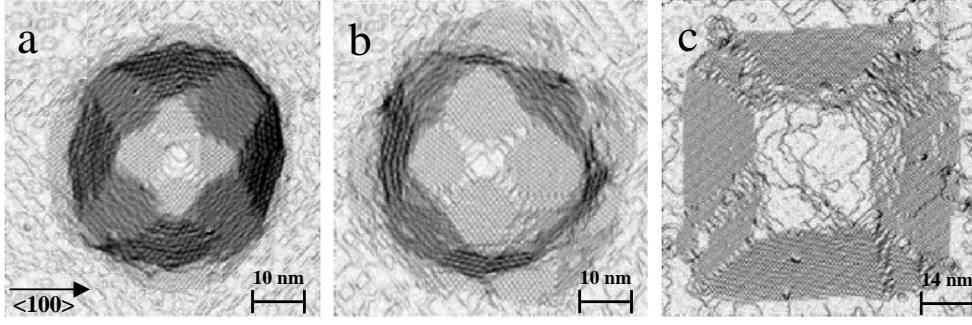
Figure 4.5: STM images showing the different changes undergone by Ge "domes" during Si overgrowth. a) As-grown Dome. b) After depositing 1 ML of Si, the shallow (105) facets on top of the islands are substantially enlarged. c) After depositing 4 ML of Si, a flat (001) surface is formed on the islands top. (Images courtesy of A. Rastelli. [70])

energetic cost) in favor of the shallower ones. This is efficiently done by transferring material from the top to the bottom of the island, as schematically shown in Fig. 4.4. This explains why after the deposition of 1 ML GaAs, the InAs QD shows extended (137) facets (Figs. 4.3b and 4.3c) and experience a strong height decrease (Fig. 4.2b). By depositing further amounts of GaAs the small steep facets that still are visible after the 1 ML capping, disappear completely and the continuous reduction of strain energy starts to favor (001) facets on the island top, as can be seen in Figs. 4.3c and 4.3f.

These shape transformations are quite similar to those taking place during the overgrowth of large multifaceted Ge dots (see chapter 5 for a description of these dots). As shown in Fig. 4.5, dome islands undergo a sort of backwards evolution into transition domes, pyramids, transition pyramids and prepyramids, when being overgrown with Si [70]. The as-grown dome islands displayed in Fig. 4.5a are composed by four (113) and eight (15 3 23) facets laterally bounding the dot and by four (105) facets that form its apex (see also Fig. 5.1). When these are capped with 1 ML of Si, their height decreases by $\sim 20\%$ and the (105) top facets increase their extension while the steeper (113) and (15 3 23) facets are drastically reduced (see Fig 4.5b). Finally, after covering with 4 ML of Si, the islands evolve in truncated (105)

pyramids with a flat (001), see Fig. 4.5c [70].

The comparison of Figure 4.3 and Figure 4.5 clearly shows that the same type of morphological transformations takes place in the two material systems. In fact, every shape adopted by the capped Ge dots has its equivalent for the capped InAs dots, and the small and large QDs described in chapter 3 can be considered as the equivalents of pyramids and domes in the Ge/Si(001) system (see chapter 5). Indeed for both material systems, small "hut" islands (composed by one type of shallow index facets), and larger "domes" multifaceted islands (composed by steep facets bounding the island body and shallow ones at the apex) are formed. Furthermore, these experimental observations confirm the theoretical model described by Daruka *et al.* [75], in which basing on the minimisation of surface and volume strain energy, these authors predicted island equilibrium shapes that become steeper with increasing volume and that nicely agree with the experimental ones reported here. Even the presence of shallow facets at the base of the domes, that was added to the model later [?], is actually observed in both material systems (Figs. 4.3a and 4.5a).

We incidentally noticed that the Ge transition dome showed in figure 4.5b is very similar to the transition islands that form during the pyramid to dome transformation (see next chapter, Fig. 5.4e). Therefore, based on the analogy described before, we can predict that the equivalent intermediate dots that will form in the InAs/GaAs(001) case as transition states between small and the large islands, will be very similar to the 1 ML capped structures in Fig. 4.3b. Although we do not have any direct evidence of such structures, recent reports by Salamo *et al.* [74] can be interpreted in this light.

4.2.2   Second regime: True overgrowth process

The height and shape transformations that we have just described, are mainly caused by a transfer of material from the dot top to its bottom. Contrarily to the Ge/Si(001) case in which the surface diffusion is high enough to redistribute this material smoothly over the whole plane, in the case of InAs/GaAs(001) a large fraction of the dot material remains close to its foot. This effect can already be seen in Fig. 4.1b

for the deposition of 1 ML of GaAs and becomes absolutely evident in Fig. 4.1c in the form of two shoulders elongated in the $< 1\bar{1}0 >$ direction (3 ML of GaAs). The deposition of a GaAs cap thus reduces the height of the dots but contemporary creates lateral shoulders with an increasing height. A critical thickness is naturally defined as the situation in which these two oppositely moving fronts meet. Following the evolution series in Fig. 4.1, we see that this happens after depositing around 4 ML, i.e. exactly when the morphological parameters in Fig. 4.2 show their transition. From this point on, the overgrowth mechanism has inevitably to change, since the original QDs is no more protruding from the surface but is completely embedded within the shoulders. The mechanism of local intermixing and strain release that characterized the first time regime are no longer active, so that also the morphological evolutions that derived from them can no longer take place.

In fact, after the amount of deposited material has exceeded the critical thickness, no strong shape changes are observed and mainly only size changes are evident (Fig. 4.1d-f). The overgrown structures elongate and become higher with a rate that linearly increases with the amount of deposited GaAs (see Fig 4.2b). Their anisotropic shape is caused by the anisotropy in atomic diffusion on the GaAs(001) surface that shows a ~ 100 times lower barrier along the $< 1\bar{1}0 >$ direction than along $< 110 >$ [76]. In conclusion, in this second regime, a true overgrowth takes place with the material being simply deposited on top of the pre-existing structures, whose morphology is almost self-similarly reproduced.

In order to investigate the possible influence of kinetic limitations on the QD capping, we performed overgrowth experiments using two different deposition rates. For these experiments two series of samples containing nominally identical free-standing islands were overgrown with the same amounts of GaAs (1-11 ML), but using fluxes of 0.08 and 0.6 ML/s respectively. The variation of the dot height with the amount of deposited GaAs can be seen for both series in Fig 4.6. These plots show that also in the case of a higher deposition flux the overgrowth is characterized by two different regimes: a first one in which the height of the dot decays almost linearly, followed by a second regime where the height of the overgrown structures, increases
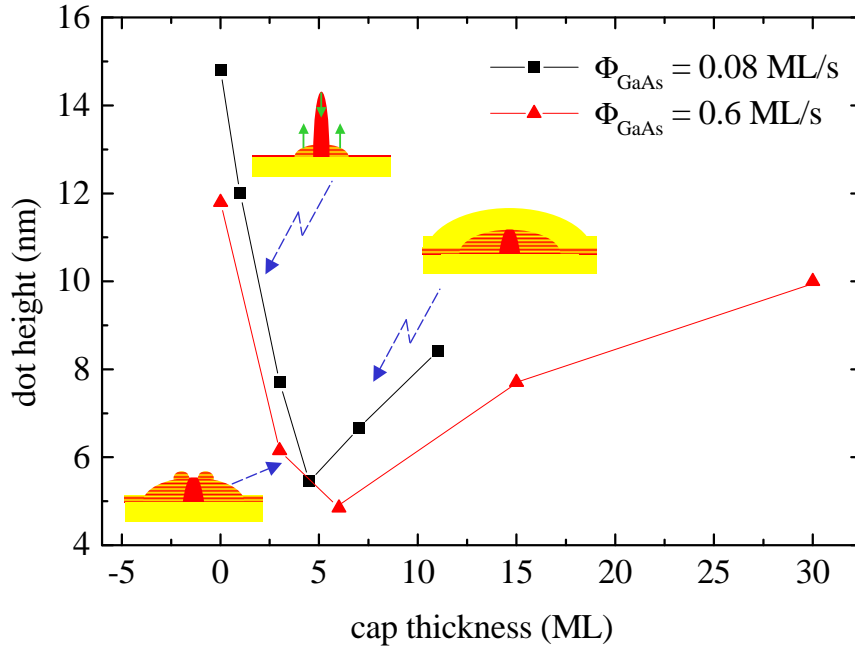
Figure 4.6: Evolution of the dot height as a function of the capping layer thickness for two different deposition rates (the heights are measured in respect of the original position of the wetting layer). The occurrence of two overgrowth regimes is observed: a first rate-independent linear height decay, followed by a second rate dependent true overgrowth. The lines connecting the experimental data are only eye guides. Schematic representations of the overgrowth morphologies are shown as insets.

monotonically. In case of a capping thickness of 3 ML GaAs, see figs. 4.7a, just slight differences in the lateral size characterize the dots overgrown at low or high rates. They seem to have undergone similar processes, since both present the same features, being elongated in the $< 1\bar{1}0 >$ direction and having a small remanent part of the original dot protruding from their center. This confirms that kinetic effects are not playing a critical role in the first regime, and strengthes the statement that the shape transformations occurring before the critical thickness are mainly thermodynamically driven.

In the second regime a striking difference is observed between the dots covered at high and low GaAs deposition rates. In figures 4.7c and 4.7d, STM images corresponding to a coverage of 15 ML of GaAs are shown. If a lower flux is used, large
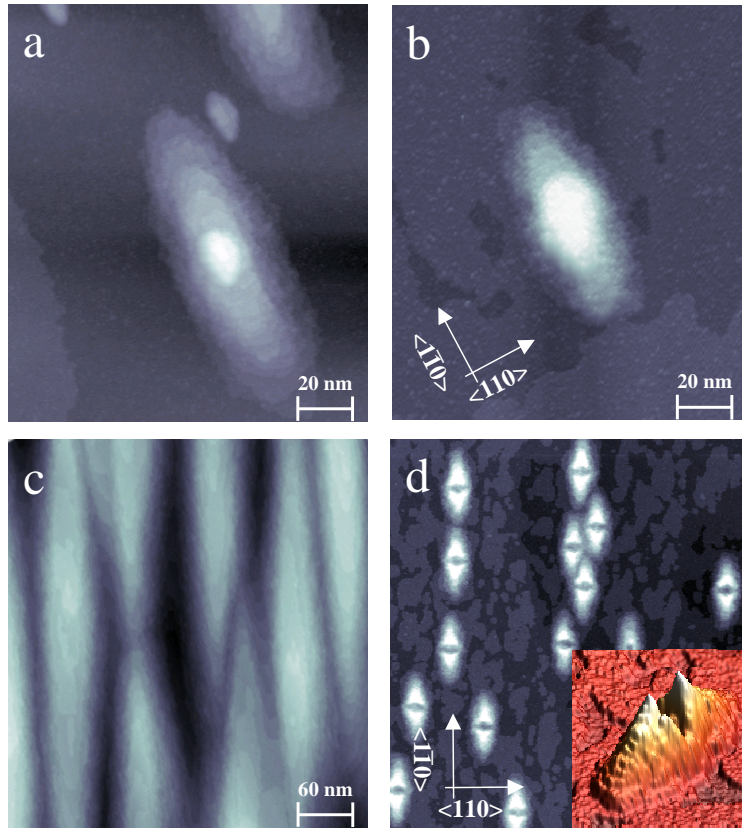
Figure 4.7: STM images of nominally similar QD samples overgrown with the same amount of material, but at different deposition rates: 0.08 and 0.6 ML/S for the left and right column respectively. Images (a) and (b) show QDs covered with 3 ML of GaAs, (c) and (d) after the deposition of 15 ML of GaAs. The inset in (d) is a 3D representation of one of the humpback structures (see text).

structures ($L > 400$ nm) are formed, that do not present any feature of the original dot but preserve the elongated hill-like morphology of the critical thickness stage. In contrast, at higher fluxes, nanostructures with a completely different morphology develop (see Fig. 4.7d), having a rhombus base and a depression at their center that gives to the growth front the appearance of camel humpback (inset in Fig. 4.7d).

In order to understand the origin of the strong differences between the samples overgrown at low and high deposition rate, it is helpful to analyze with higher precision the morphology of the overgrown structures around the critical thickness. In
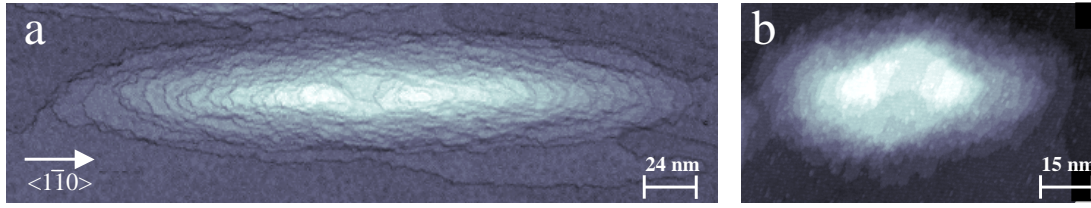
Figure 4.8: STM image of QDs capped with 4.5 ML of GaAs. The formation of a ridge in the center of the dot is observed independently of the deposition rate used during the overgrowth: (a) low rate (0.08 ML/s), (b) high rate (0.6 ML/s).

fact, up to this GaAs coverage the two flux series behave almost identically and only from here on they start to follow different evolution paths.

4.2.3   Critical thickness: Ridge formation

A closer look at the structures that develop after the deposition 4.5 ML GaAs, i.e. just after the critical thickness, reveals the formation of two ridges symmetrically located in respect to the original QD position (see Fig 4.8). Their development is independent of the deposition rate but the ridge separation appears to be larger for the lower rate (compare Figs. 4.8a and b).

By carrying on with the capping, at low deposition rates the ridges disappear and only the $< 1\bar{1}0 >$ elongated morphology remains and extends (Figs. 4.1d and f). On the contrary, when depositing GaAs at 0.6 ML/s, the ridges continue developing and finally evolve into the camel humpback structures of Fig. 4.7d. This dichotomy clearly derives from stronger or weaker kinetic limitations: at low GaAs rates the growth front has enough time to minimize it surface extension and therefore to smooth out the ridges, while at high rates the smoothing effect of surface diffusion is reduced and the morphological modulations are rather reproduced by the growth front [77].

These considerations account for the difference in the overgrown structures shown in Fig. 4.7, but the origin of the ridges in Fig. 4.8 has still to be explained. For this we have to remember that the morphological transformations that InAs QDs undergo in the first capping regime, mainly depend on the segregation of In and on
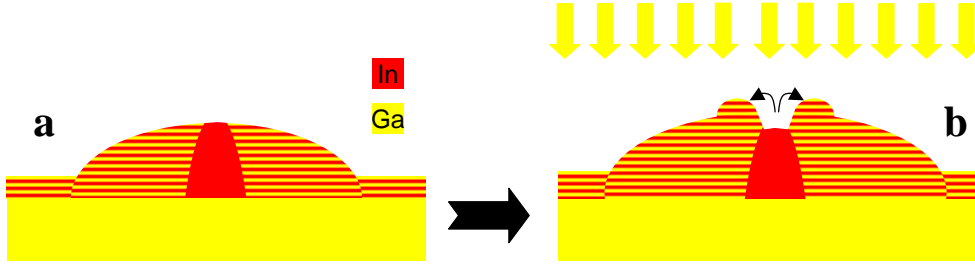
Figure 4.9: Sketch illustrating how the ridge is formed: a)cross section of the overgrown dot immediately before the critical thickness is reached. The inhomogeneous composition of the dot is represented. b) The ridge is formed due to the diffusion of atoms away from the center of the dot, in addition with the incoming atoms. That results in a higher effective flux in the region around the center.

the resultant local incorporation of Ga atoms within the QDs. The crucial point is that, even before capping, nominally pure InAs QDs are actually characterized by a vertical compositional gradient [78, 79], whit a high Ga content close to the dot base (Ga percentage up to 60% have been reported at a height of 3 nm above the WL [80]). The probability of incorporating Ga atoms of the incoming flux therefore depends on which part of the original QD is uncovered and will diminish with the decrease of the dot height. At certain point, the incorporation of Ga will almost completely stop and from here on, the Ga atoms that are directly deposited onto the dot will simply diffuse away from it and stick to the lateral shoulders. In fact, these will always have a lower In content than the dot and therefore have a smaller lattice parameter and represent a better adsorption site for Ga atoms, because of a lower lattice mismatch. For our experimental conditions, this stop evidently happens around the critical thickness, and the ridges of Fig. 4.8 are actually the result of the Ga-rich material that diffuses away from the dot center.

We notice that the already cited experiments by Songmuang *et al.* [67], further support this picture. In fact when overgrowing with $In_xGa_{1-x}As$ instead of GaAs, the capping thickness at which the Ga incorporation (and therefore also the dot height decrease) stops, will be smaller. From this point on, as we have already said,

the overgrowth will proceed in an almost conformal way. This is actually confirmed by the experiments in [67], where overgrowth structures were reported with a central remaining part of the original dot that sticks out of the lateral shoulders for capping thicknesses > 15 ML. Moreover Songmuang et al. also showed that the height of the dot increases with the percentage of In in the capping flux.

Chapter 5

Ge quantum dots

5.1 Introduction

The growth of Ge and SiGe alloy films on Si(001) substrates has become a subject of considerable technological interest over the last decade, since carefully controlled growth of strained, defect-free SiGe has given rise to the unexpected improvement in the performance of pure silicon-based heterostructures.

Silicon and germanium are miscible over the entire binary alloy composition range, showing a nearly ideal solid solution behavior. Therefore, by changing the alloy ratio in heterojunctions made of GeSi/Si, it is possible to tune the strain between the materials and to reengineer the band structure of silicon. This allows, for example, to enhance the carrier mobility and to increase the wavelength, without generating lattice defects [81, 82]. In contrast to traditional silicon-based devices, SiGe ones can reach speeds up to 120 GHz, (which is an increase by a factor between 2 and 4) approaching the best attainable values in III-V heterostructures. These improvements result into high-frequency operation devices at lower production costs, because chipmakers can run the GeSi technology on existing state-of-the-art silicon production lines by implementing minimal changes and retooling. These features have boosted the use of GeSi into communication and other high-speed electronics markets, traditionally thought of as GaAs strongholds [83].

On the other hand, nanostructures fabricated from a material system such as
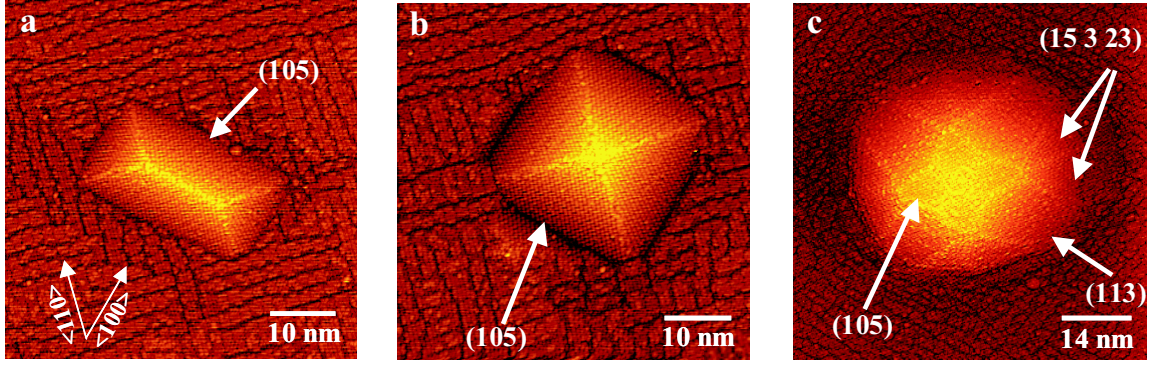
Figure 5.1: High resolution STM images of Ge dots showing the three shapes typically found in growth experiments of Ge on Si(001): (a) hut-like island, (b) squared based pyramid and (c) dome-like island. The characteristic (NxM) surface reconstruction of the WL is also visible.

Ge/Si offer some advantages compared with other heteroepitaxial systems (e.g. InAs/GaAs). That is because the epitaxial deposition of Ge/Si heterostructures can be regarded as a simpler model for strained layer epitaxy and self-assembly techniques, compared with complex systems where more than two compounds are used [84]. Thus the growth of GeSi on Si over a wide range of alloy concentrations is of interest to both technological and scientific communities.

Si and Ge are qualitatively quite similar in their structural and electronic properties: both present the diamond crystal structure, but the Ge lattice is expanded by 4.2% with respect to the Si lattice and the Ge-Ge bond is weaker than the Si-Si one, leading to a smaller surface energy. Consequently the Ge/Si heteroepitaxial system has often been discussed as a classical model for the Stranski-Krastanow growth-mode. Prior to the mid-1980s, a simple picture was generally assumed in which a smooth pseudomorphic Ge wetting layer grows up to a certain thickness and is followed by the growth of dislocated 3D clusters. It was just until 1990, that this nonplanar growth was revisited and exploited, mainly due to the efforts of Eaglesham and Cerullo [15]. These authors showed that the islands that form in the initial stages of clustering are actually coherent with the substrate, that is, without dislocations. In the same year, Mo *et al.* [85] precisely elucidated the morphology of such islands with atomic resolution. Since then the interest in this particular system has dramatically

and steadily increased.

5.2   General aspects of Ge islands on Si(001)

The 4.2% misfit strain in the Ge/Si(001) system induces the spontaneous formation of three-dimensional faceted islands after the growth of a 3 to 4 monolayer thick wetting layer [86]. Depending on the deposition parameters, different type of coherent islands develop, as shown in Fig. 5.1. At low growth temperatures rectangular-based islands, so called "huts", are formed (see Fig. 5.1a). Their principal axes are strictly aligned along the orthogonal $\langle 100 \rangle$ directions and their facets follow the (105) orientation, making a shallow angle ($\sim 11°$) with the Si(001) plane [85]. At higher temperatures the coexistence of two different island shapes occurs with a morphology that depends on the island size. The smaller islands are squared-based pyramids bound by (105) facets (see Fig.5.1b), whereas the larger ones are multifaceted islands (so called "domes"), which have a larger aspect ratio and include steeper facets such as (113) and (15 3 23) [87]. The same type of islands are also formed when, instead of pure Ge, a GeSi alloy is deposited, although in this case the length scales are expanded because of the reduced misfit strain [88].

This bimodal distribution of sizes is observed over a wide range of growth conditions, with pyramids occupying the lower peak of the volume distribution and the domes occupying the higher peak [17, 70, 87]. The existence of the two island families is consistent with thermodynamic arguments, predicting that their shape is determined by the competition between surface energy and strain relaxation. An island with steeper facets and higher aspect ratio (height/base) relaxes more strain, but has more surface area than one with a comparative lower aspect ratio [75, 89].

Some models have been proposed for explaining the transition between low-volume pyramids to high-volume domes [87, 90, 91], but at present a clear explanation of the atomic processes driving this transformation is still lacking. Just recently, experiments where the shape change from pyramids to domes was observed during growth, have been reported by Ross *et al.* [91]. These authors performed real-time low energy
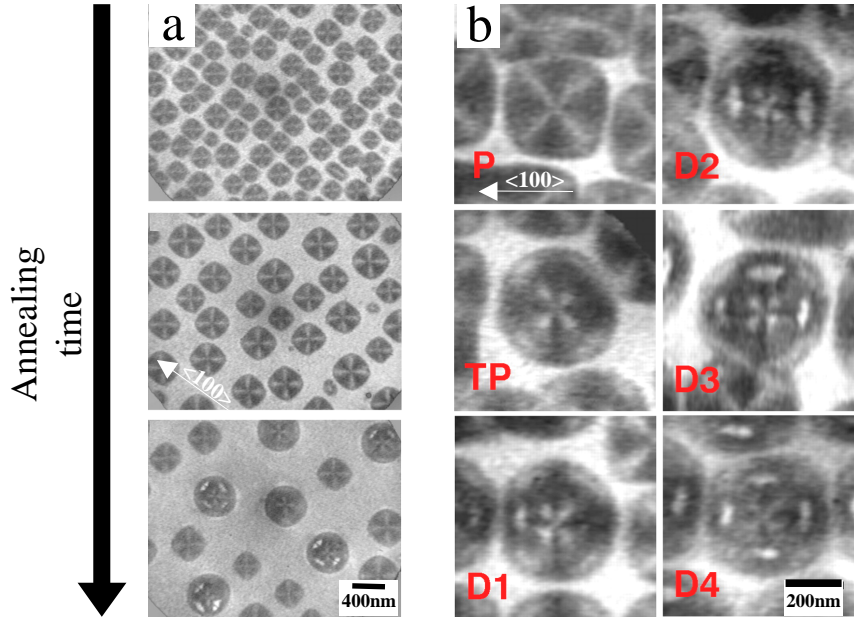
Figure 5.2: Real-time low-energy electron microscopy (LEEM) images showing the pyramid to dome transition in the GeSi/Si(001) system: a) during postgrowth annealing experiments (30 min. to 6hrs), the shape transition is accompanied by a gradual reduction in the island density, and b) during the growth, the different transformations (TP,D1,D2,D3) undergone by the original pyramid (P) to convert in a full shaped dome (D4). (see ref. [91])

electron microscopy (LEEM) measurements during sample growth and postgrowth annealing (see Fig. 5.2a), and showed that pyramids undergo several intermediate morphological changes before transforming in multifaceted dome-like islands. These observations indicate that the shape modification occurs continuously, discarding the possibility of an abrupt phase transition, as proposed by Medeiros-Ribeiro *et al.* [87]. Although the resolution achievable by the LEEM technique (~ 5 nm) allows to observe in real time the formation of different transition islands and to sketch their shapes (see Fig. 5.2), it is not enough for getting precise information about their shape and for understanding the fundamental processes that underlie the transition.

With the aim getting a better interpretation of the mechanisms that produce the shape change, we performed an extensive analysis on postannealed samples (where the pyramid to dome transformation has already taken place) by means of high resolution
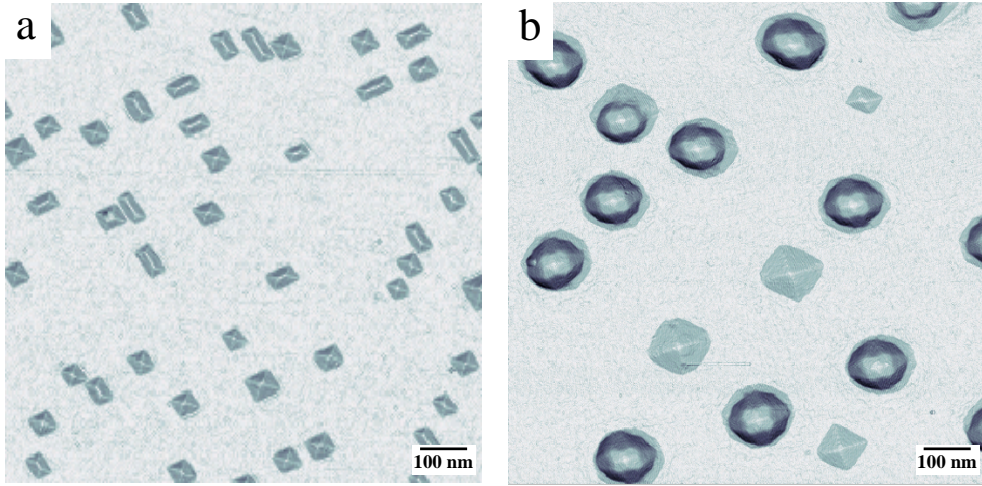
Figure 5.3: 1x1 μm^2 images of Ge islands, formed after the deposition of 6 ML of Ge on Si(001) at 560°C. (a) As-grown and (b) after annealing for 600 sec at 560°C.

STM. Based on these experimental data and on atomistic arguments derived from recent theoretical investigations, a simple model that captures the essential features of the transformation is also presented. Additionally, selective etching experiments were conducted in order to determine the chemical composition of the islands during the various phases of the transition.

5.3 Pyramid to dome shape transition of Ge QDs

All the samples used in the experiments described in this chapter were grown by solid-source molecular-beam epitaxy on Si(001) substrates. The growth procedure was as follows: the samples were chemically cleaned, introduced in the MBE chamber and deoxidized at 950°C. After the deposition of a 100 nm Si buffer layer (growth rate of ~ 1 ML/s), self-organized, coherent islands were formed by depositing 6.0 monolayers of germanium at a growth rate of 0.05 ML/s. Subsequently, these samples were annealed at the growing temperature (560°C) for different time intervals (0-1200 sec) and then transferred to the UHV-STM system after cooling to room temperature. Figure 5.3a, shows an as-grown sample where small pyramids and elongated hut islands, typically formed under these growth conditions are observed ($\sim 1.2 \times 10^{10}$

cm^{-2}). If immediately after the islands formation a growth interruption of 600 sec is applied, an abrupt reduction in the island density to the values of $\sim 5\mathrm{x}10^9 cm^{-2}$ is observed. Additional experiments in which longer annealing times are used (900 and 1200 sec), show similar island morphologies, sizes and densities.

A detailed analysis of STM images similar to Figure 5.3b reveals the presence of hybrid structures that coexist with pyramids and domes, and have features that belong to both types of islands. We interpreted these hybrid islands as the intermediate states in the shape transition from pyramid to dome. The fact that during the sample cooling the quenching rate is very slow ($\sim 1°C/s$) and that the transition islands are formed independently on the annealing time, suggest that these islands probably are thermodynamic metastable minima in this transition, rather than the result of frozen kinetics.

Images in Fig. 5.4 correspond to different islands found on the same sample (annealed for 600 sec). It can be noticed that these images are a sort of high-resolution version of the on-line results obtained by Tromp (shown in Fig. 5.2b). Therefore, the sequence in Fig. 5.4 can be interpreted as the actual pathway followed by the pyramids in their way to transform in domes.

The reduction in island density during annealing indicates that a coarsening process takes place, i.e. some islands disappear and others increase their size, as shown in the real time experiments by Ross *et al.* [91]. Therefore the shape transformation is actually a size increase, in which the material is supplied by the disappearing islands and probably from the WL. This size increase does not happen due to global transformations of the islands, but through the material that is subsequently added to the existing island, so that it can be though as an overgrowth. This is because at the used annealing temperatures, while surface process are highly active, bulk processes are almost inactive.

A detailed description of the morphological changes undergone by the islands shown in Fig. 5.4 is given as follows. Initially the huts increase their size by means of a conformal overgrowth process (complete facet layers are formed) that maintains the (105) facet orientation (Fig. 5.4a). This conformal transformation does not
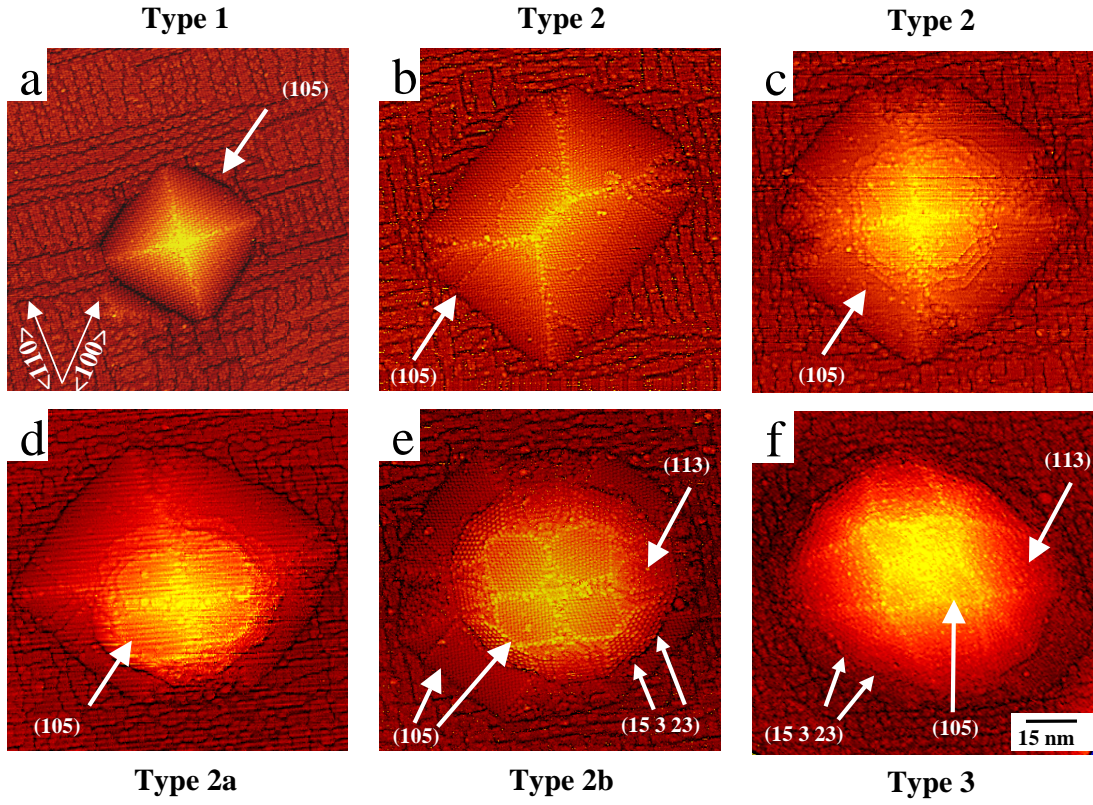
Figure 5.4: High resolution STM images of representative islands corresponding to different stages of the morphological transition: (a) pyramids (type 1), (b) pyramids where the first incomplete layers are observed (type 2), (c) and (d) pyramids with several incomplete facets grouped at the top (type 2a), (e) islands where new facets are formed (type 2b) and (f) almost complete and fully complete domes (type 3).

continue indefinitely but stops after certain critical size is reached, indicating that there exists a maximum size for the pyramids. From this size on, incomplete facet layers are formed (Fig. 5.4b). This type of non-conformal overgrowth is doubly inhomogeneous: horizontally and vertically. Horizontally, because the corners of the pyramids are not more covered. Vertically, because incomplete facets are formed and remain confined at the top of the island. The number of incomplete facets increases with the island size (Fig. 5.4c). These incomplete facets are bound in their lower part by steps that accumulate and get continuously closer (Fig. 5.4d). At certain point, this high density of steps prefers to bunch together in order to minimize the
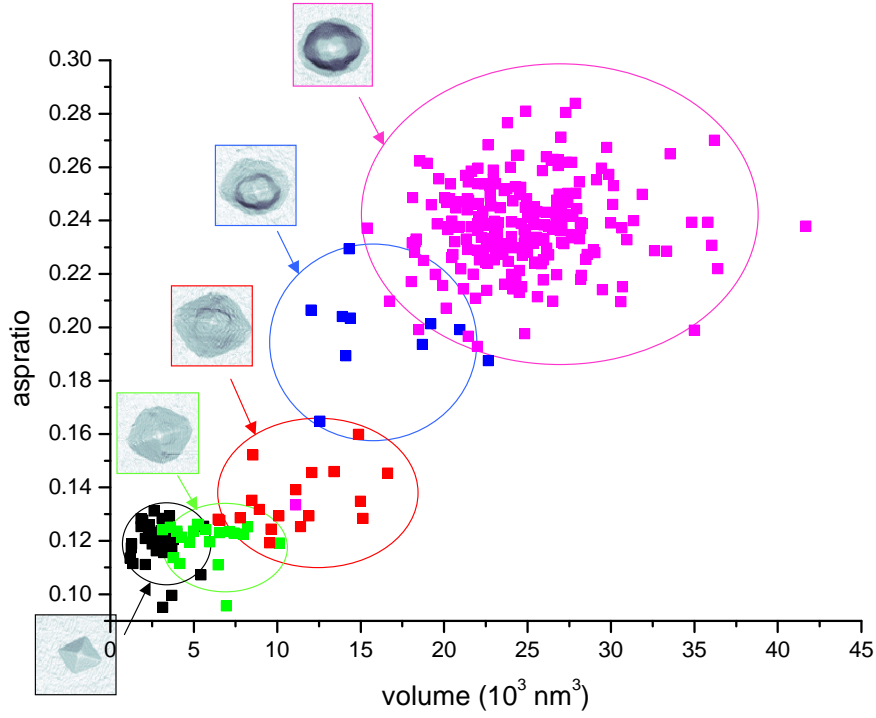
Figure 5.5: Scatter plot showing the island aspect ratio as a function of their volume. All annealed samples are considered (600, 900, 1200 sec) and the island type, defined according to Fig. 5.4, is indicated a color code.

surface energy. This step bunching produces new facets: a pair of (15 3 23) facets is formed symmetrically around the $< 100 >$ directions and a (113) facet along the $< 110 >$ directions (Fig. 5.4e). By increasing the amount of material that joins the island, these new facets increase their extension and extend almost completely down to the island foot. The shape transformation is complete and a full dome is formed (Fig. 5.4f).

The pyramid-to-dome transition (with qualitatively the same transition islands shown in Fig. 5.4) is also observed after depositing more than 7 ML of Ge at 560°C (without any postgrowth annealing)[92, 93]. This indicates that the shape transition, that can be considered as a size increase, has its origin only on the material redistributed during island coarsening.

In order to get quantitative information of the island size evolution during the transition, an evaluation island-by-island is done. This evaluation was performed for

the as-grown samples as well as for the annealed ones (plots with different colors). The results of that analysis are shown in Figure 5.5 in the form of a scatter plot, where variation of the island aspect ratio with respect to its volume is plotted. For this analysis, the aspect ratio was defined as the quotient of the height to the square root of the base area and only for the as-grown sample (characterized by asymmetric islands) was set as the quotient of the height to the half of the shortest base length. In this way the aspect ratio for pyramid and huts is the same.

The islands (Fig. 5.4) have been classified in different types depending on the transformation stage they are. This classification is used for identifying the different type of islands in the scatter plot shown in Fig 5.5. This Figure clearly shows that the islands cluster into two distinct groups at the extremes of the scatter plot, that correspond to the pyramids and domes respectively. The region in between is occupied by transition islands that are at different stages of the transformation, that is similar to what reported by Medeiros-Ribeiro *et al.* [87]. It is noteworthy that independently on the annealing time, all the samples present on average the same morphological evolution. This can be explicitly seen in Fig. 5.6a, where the distribution over the different island types appears clearly to be almost identical for the samples annealed for 600, 900 and 1200 s.

The careful identification of the individual island type done in the scatter plot of Fig. 5.5, allows to precisely identify the critical volume after which the pyramids stop to grow in a conformal way. The size of the largest pyramid that does not show any sign of incomplete facets can indeed be obtained by zooming into the aspect ratio scatter plot (see Fig. 5.6b) and, for the chosen experimental conditions, that corresponds to a base of ~ 45 nm.

The analysis done in Fig. 5.6b also shows that the pyramid-to-dome transition starts much more smoothly and earlier than what has been repeated so far in literature [87, 70], representing another piece of evidence against its interpretation in terms of an abrupt thermodynamic phase transition. Strong aspect ratio modifications happen only later in the transformation pathway, when the bunched steps of the incomplete facets transform in steeper (113) and (15 3 23) facets (see Figs. 5.5 and 5.4e).
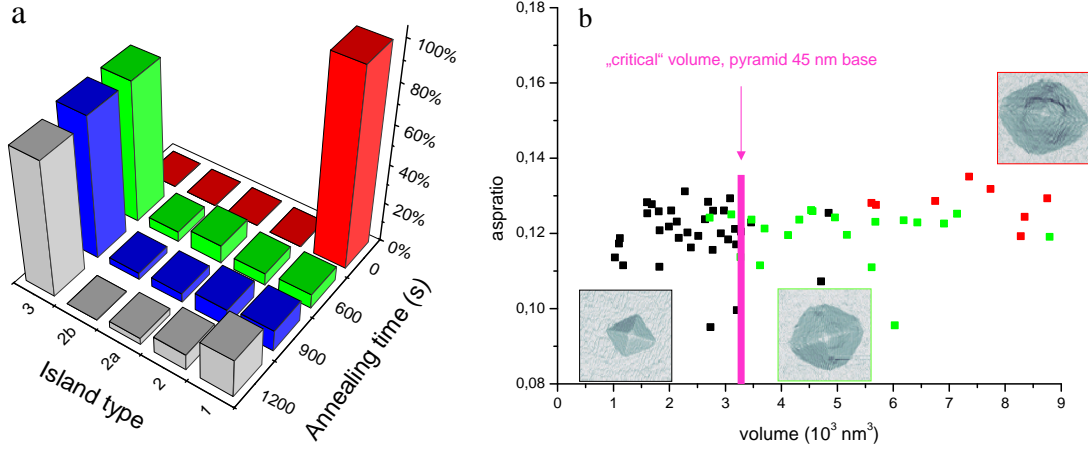
Figure 5.6: (a) Dependence of the island type distribution (in percentage) on the annealing time. (b) Close up of the scatter plot shown in Fig. 5.5, from which the critical volume for the pyramid-to-dome transition can be determined.

5.4   Understanding the cap formation

In order to determine whether if these transition islands are the result of kinetic and/or thermodynamic processes, a model based on results from first principle calculations, molecular dynamics simulations and energetic considerations was developed in collaboration with the theoretical group of the University of Milano-Bicocca (Italy), headed by the Prof. Leo Miglio. In particular, this model is committed to explain the cap formation and in spite of its simplicity, captures the essential features of the experimentally observed shape transition: islands smaller than a certain critical size grow in a conformal way (full facet formation), while bigger islands start forming a cap at their top (incomplete facet formation). The full pyramid-to-dome transition is clearly much more complex and involves the bunching of the steps that delimit the incomplete facets and the further evolution of these bunches into steeper (113) and (15 3 23) facets. Nevertheless, this model accounts for the key processes of the transformation, namely the change in growth mode.

Recently, *ab initio* [94, 95] calculations have shown that the (105) surface of Ge, although being a vicinal of the singular (001) orientation, is basically flat because of its peculiar surface reconstruction that eliminates the (001) steps. As a consequence,
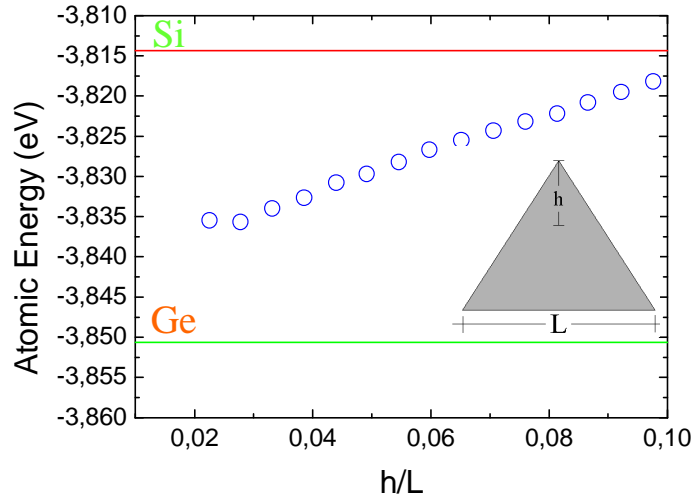
Figure 5.7: Adsorption energy (per atom) on a 27 nm wide Ge(105) pyramid as a function of h/L (height/base length). Bulk Ge and Si values are showed as references. Data courtesy of F. Montalenti [96].

no step edge barriers hamper the atoms movement, so that atom diffusion turns out to be almost isotropic. Moreover, these calculations estimated values for the in-plane diffusion barriers on Ge(105) of about 0.6 eV, implying that at our experimental temperatures (560°C) diffusion on the pyramid facets is not only isotropic but also extremely fast. Therefore, the transition morphologies that we observed experimentally can not be interpreted as the result of a frozen kinetics. On the other hand, a full thermodynamic approach is also not appropriate, since at 560°C bulk diffusion is still inactive, so that not all the possible system configurations are actually reachable. Most probably this means that the shapes adopted by transition islands correspond to metastable thermodynamic minima compatible with an adatom diffusion limited to surfaces.

In order to determine the energy of the different surface configurations, we have first to evaluate the adsorption energy of a single Ge atom on a (105) pyramid [1]. For this purpose, molecular dynamic simulations of Ge(105) pyramids with realistic

---

[1]In the following we will adopt the simplified assumption that the QD structures are composed only by Ge. We expect that a more realistic treatment considering a GeSi composition will not change substantially our conclusions.
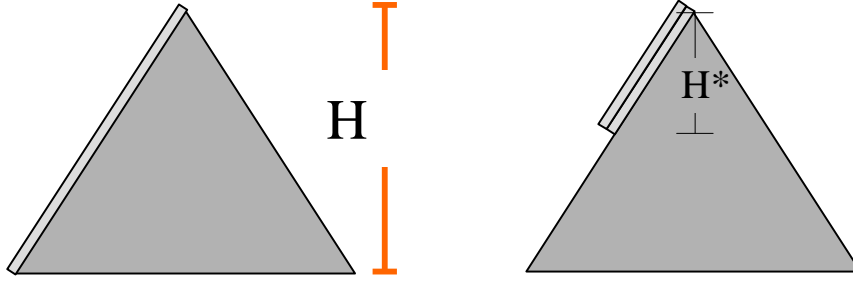
Figure 5.8: Schematic representation of the complete and incomplete facet configurations considered in the model of section 5.4.

sizes have been performed. The atomic interactions were computed according to the Tersoff potential, which allows a good description of the elastic properties of Si-Ge compounds (further details can be found in ref. [95]).

These calculations show that the energy per adsorbed atom is a linearly increasing function of the pyramid height (see Fig. 5.7). This is a direct consequence of the vertical relaxation of the lattice parameter that, on the top of the islands, approaches the Ge bulk value. In other words, atoms close to the island top occupy energetically more favorable sites than those at the island bottom.

By considering only the adsorption energy, one would predict a material accumulation on the upper part of the pyramids. This does actually not happen, at least during the initial stages of the pyramid growth, because the formation of incomplete facets requires the creation of energetically unfavorable steps. Nevertheless, the experimental data in Fig. 5.4b and 5.6b show that after a certain critical volume is overcome, incomplete facets start to form. By using the calculation results in Fig. 5.7, we can now quantitatively evaluate the energy of these two configurations (schematically represented in Fig. 5.8) in order to estimate the preferred one. We notice that, the trend of the atomic energy shown in fig. 5.7, although was computed for a 27 nm wide pyramid, is also valid for pyramids of arbitrary size, since the calculation demonstrated a self-similar behavior [96].

As a consequence, the energy gain for covering a unit of surface area of a (105)Ge

pyramid can be written as:

$$E_{surf}(h) = -\gamma_o + a \times \frac{h}{L}, \tag{5.1}$$

where γ_o is the surface energy of a fully relaxed (105)Ge surface, h is the height on the pyramid measured form its top and a is a proportionality constant obtained from the data in Fig. 5.7. With this expression, the total gain in energy obtained by forming a new complete layer on the pyramid facet (see the left panel in Fig. 5.8) is given by:

$$E_0^{tot} = \int_0^H E_{surf}(h)d\gamma(h) = -AH^2 + BH^3, \tag{5.2}$$

where A and B depend on a and γ_o, and contain the geometrical factors of the integration. The alternative configuration (see the right panel in Fig. 5.8) is obtained by arranging the atoms of all full facet into N incomplete facets. For a matter of simplicity, we supposed that they have all the same height $H^* = H/\sqrt{N}$ (see Fig. 5.8). In this case, the total energy is given by a sum of the surface energy and the energy of the steps that delimit the lower part of the incomplete facets:

$$E_N^{tot} = \int_0^{H^*} E_{surf}(h)d\gamma(h) + 10H\Gamma/\sqrt{N} = -AH^2 + BH^3/\sqrt{N} + CH, \tag{5.3}$$

where Γ is the step energy.

The most favorable configuration is determined by sign of the difference between the energy of these two configurations:

$$D_0(N) = E_0^{tot} - E_N^{tot} = B'(N)H^3 - C(N)H \tag{5.4}$$

The dependence of the energy gain difference on the number of incomplete N facets is plotted in Fig 5.9a, for three pyramids with different lateral sizes ($L = 30, 60, 90$ arbitrary units). For the smallest pyramid (green curve), $D_0(N)$ is always below negative and therefore the formation of complete facets is the energetically favored configuration. For the other two pyramid sizes however, positive values of $D_0(N)$ are obtained for almost every value of N. The actual island shape is determined by the largest volume of the energy gain i.e. by the number of incomplete facets
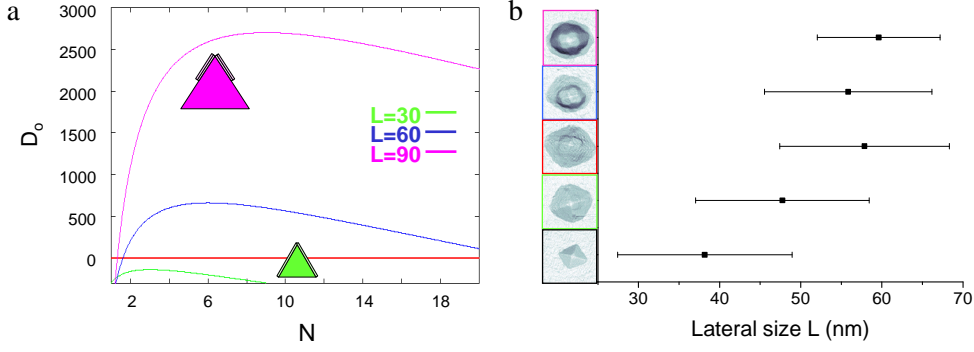
Figure 5.9: (a) Energy difference D_0 between the incomplete and the complete facet configuration as a function of the number incomplete facets N. The plots are obtained from eq. 5.4 for three pyramids with different sizes L=30, 60, 90 (arbitrary units). (b) Plot taken from experimental data showing the variation of the island lateral size with the number of steps.

N^* that maximizes $D_0(N)$. These turn out to be ~ 6 for a pyramid with a lateral size L=60 and ~ 9 for L=90. We notice that this scaling of N^* with the pyramid size reproduces our experimental observation, that the actual number of facets is an increasing function of the transition island size (see Fig. 5.9b).

5.5   Trench formation

An interesting feature of the islands obtained after the annealing experiments, is that they are surrounded by shallow depressions, also called trenches. In Fig. 5.10 an STM topography is shown, corresponding to a 600 sec annealed sample with different types of transition islands: the use of a compressed color scale enhances the visibility of the trenches surrounding every island. Other experimental groups have already reported about the formation of grooves around large Ge or GeSi islands on Si(001) [90, 97, 98], and have suggested that they could act as an effective strain-relief mechanism. Nevertheless, a precise description of their shape is missing and their origin is still under debate.

For this reason we decided to perform a detailed in-situ STM analysis of the trenches and to correlate them to the island size and morphology. In Figures 5.11a-
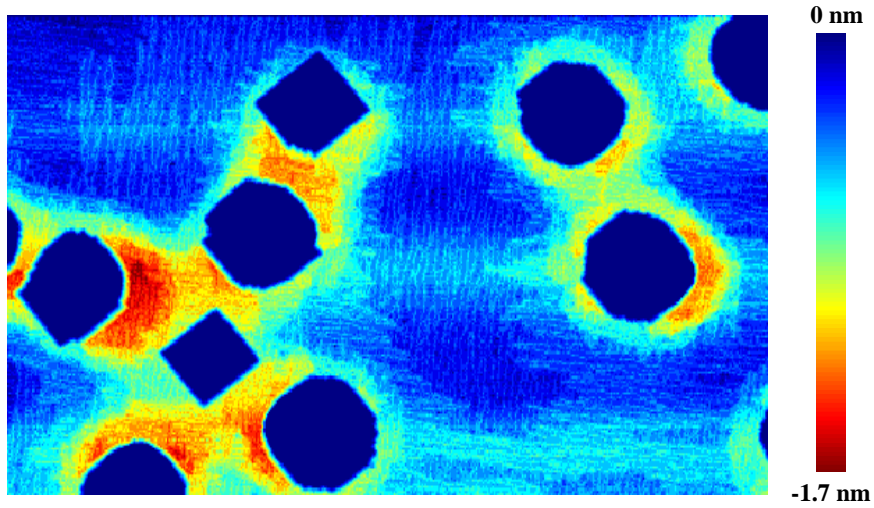
Figure 5.10: STM image of a Ge/Si(001) sample annealed for 600 sec at 560°C. A compressed color scale is used in order to emphasize the presence of trenches surrounding all types of islands.

c, enhanced color scaled images of three kinds of islands are presented: a pyramid (type 1), a transition island with incomplete facets (type 2) and a complete dome (type 3). These data clearly show that, contrarily to what stated by Chaparro *et al.*, the formation of a depression around the islands already starts for small pyramids, being in this case only one monolayer deep. The trench depth actually scales with the island size, and reaches values up to 1 nm for the largest analyzed domes. Figs. 5.11a-c quantitatively demonstrates the correlation between the trench and the island volume and also shows that there is no manifest dependence on the island type. A very similar, almost linear trend of the trench depth with respect to the island size was also reported by Chaparro *et al.*, but only for large domes, grown at temperatures higher than 600°C [97]. An other interesting aspect revealed by our high-resolution data, is that, in particular for larger islands, the trenches are not isotropic but present a four-lobe structure with a deepening along the $< 100 >$ directions. This is even clearer from the stereographic plots of Figures 5.11d-f, where the depth of the trenches is displayed in a polar representation. These plots are obtained by taking linescans that start from the dot center: the maximum trench depth along the linescan is used as radius while the angle between the linescan orientation and the $< 100 >$ direction
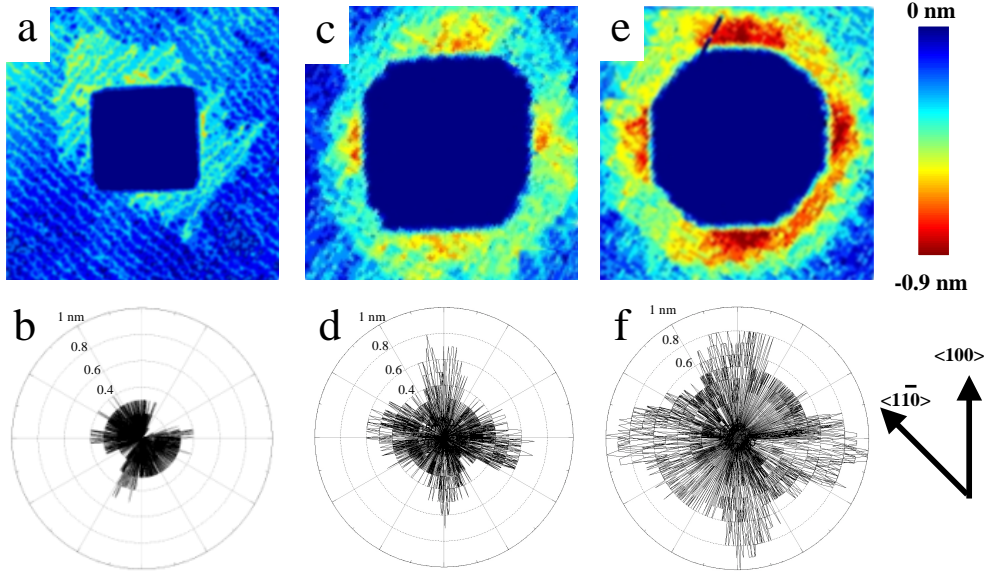
Figure 5.11: Upper row: representative STM images of isolated (a) pyramids, (b) transition island with incomplete facets, and (c) complete domes. An enhanced color scale is used in order to better visualize the trenches. Lower row: (d)-(f) corresponding polar representations of the trench depth. (see text)

is taken as polar angle [2].

By using an atomistic model, Chaparro *et al.* obtained also that the energy of lattice mismatched epitaxial islands is reduced by the formation of trenches, which thus represent an effective strain-relief mechanism. The assumptions of this theoretical model were however extremely crude (un-realistic small islands, simple harmonic nearest-neighbors interactions and a simple cubic geometry), claiming for a more precise treatment of the problem.

The collaboration with the theoretical group of Prof. Leo Miglio at the University of Milano Bicocca, allowed us to directly compare the experimental data with ad-hoc molecular dynamic simulations performed on pure Ge pyramids and domes with realistic sizes [99]. The results of these simulations are shown in Figure 5.12 where spatial maps of the zz component of the strain tensor, evaluated 3 nm below the WL surface,

---

[2]We notice that this analysis is only meaningful for isolated islands since, as seen in Fig. 5.10, trenches of neighboring islands merge and influence each other.
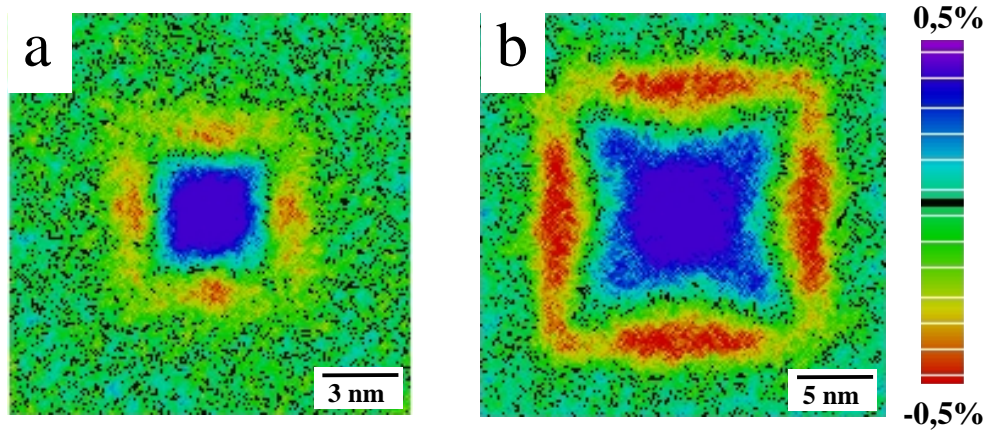
Figure 5.12: (a) Spatial maps for the zz component of the strain tensor ($\mathcal{E}_{zz}$) obtained from MD simulations of pyramids with different size: (a) 16 nm and (b) 27 nm. The maps are evaluated 3 nm below the wetting layer surface.(Data courtesy of P. Raiteri)

are shown for islands of different sizes. Similarly to what already reported in different material systems [54, 99, 100, 101], a compressed region is seen to build up in the substrate surrounding the islands. The simulations also show that the overall strain increases with increasing island size and that the strain is anisotropically distributed around the islands, with highly compressed regions close to the island edges. The correlations between these data and our experiments on the trench morphology and on the scaling of the trench depth with the island size, are evident when comparing Fig. 5.11 with Fig. 5.12. This agreement represents therefore a strong proof for the interpretation of the trenches as the result of a substrate material diffusion from higher to lower strained regions.

Figure 5.13a shows a situation that actually happens for the largest part of the transition islands: the dome-cap has developed asymmetrically. Most probably this occurs because the flux of material that arrives from the surface and produces the pyramid-to-dome transition is influenced by the random position of the neighboring islands and therefore is often anisotropic. The trench produced by such an island is deeper in the direction where the dome-cap is most developed (Fig. 5.13b). This nicely fits with the interpretation of the origin of the trenches given above, since such
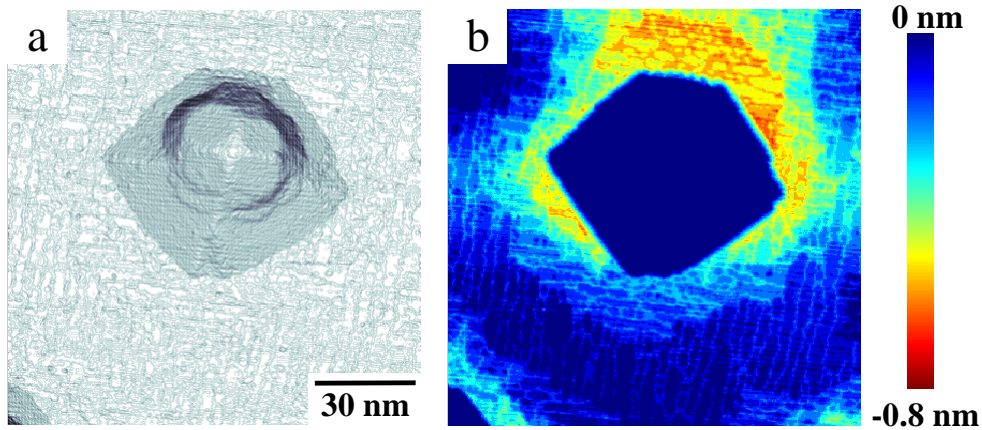
Figure 5.13: (a) Transition island where the cap has anisotropically formed. The color scale corresponds to the modulus of the local surface gradient. (b) Same image with a color scale representing the local surface height that is compressed in order to enhance the trenches. Notice that a deeper trench is formed close to the part of the island that is more similar to a dome.

an island will definitively induce a stronger compression of the substrate close to the region where its shape mostly resembles that of a dome.

Finally we have to mention that large dome-like islands grown at extremely high temperatures (850° C) also show anisotropic trenches but that, contrary to the low-temperature case, these are deeper in the $< 110 >$ than in the $< 100 >$ direction (see Fig. 5.14). The origin of this 45° rotation is still unclear but, according to our explanation of the trenches, it should be related to a corresponding change in the position of the most strained substrate regions. This could be ascribed to the extremely high Si composition of 850°C-grown domes (Si content up to 74% [98]) that would induce a strain anisotropy more similar to the Si(001) case where the maxima are actually along $< 110 >$ [102]. Further molecular dynamics simulation would help in clarifying this point.
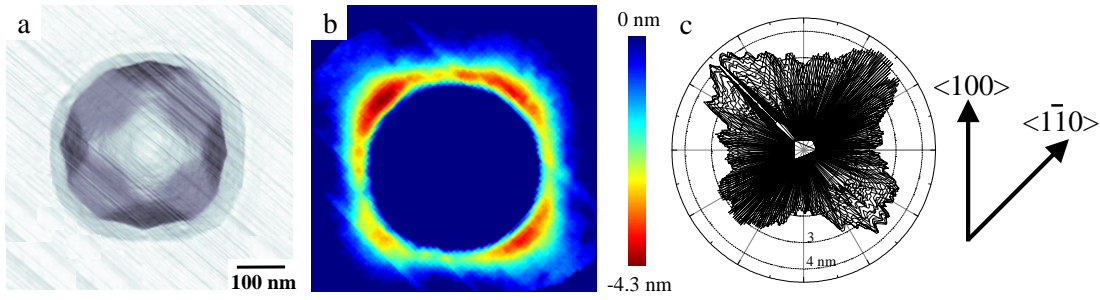
Figure 5.14: (a) AFM image of a dome island, formed after the deposition of 6 ML of Ge on Si(001) at 850°C. The colorscale corresponds to the local surface slope. The formation of a trench around this island is also observed, but with different preferential orientations in respect to the lower temperature case (560°C). Here the trenches are deeper in the $< 110 >$ than in the $< 100 >$ direction. (b) Image with an enhanced color scale in order to better visualize the trench. (c) Corresponding polar representation of the trench depth.

5.6   Island composition during the pyramid-to-dome transition

Although the optoelectronic properties of self-organized semiconductor QDs are strongly influenced both by morphology and composition, the former issue is far better understood that the latter. This is mainly due to the complications that arise when designing and interpreting sensible compositional measurements.

Most of the investigations concerning the stoichiometric structure of Ge or SiGe islands have been performed with diffractive or spectroscopic techniques that average over a large number of islands. Just recently some electron- and X-ray-microscopy-based experiments have been done for measuring compositional variations throughout individual dots [103, 104]. Nevertheless, the spatial resolution of these techniques is not high enough for a meaningful correlation with the dot morphology which, on the other hand, would be an extremely valuable information. The largest part of these experiments supports the existence of a vertical SiGe composition gradient, with most of the Si concentrated at the base of the islands.

An alternative technique that allows to get compositional information of individ-
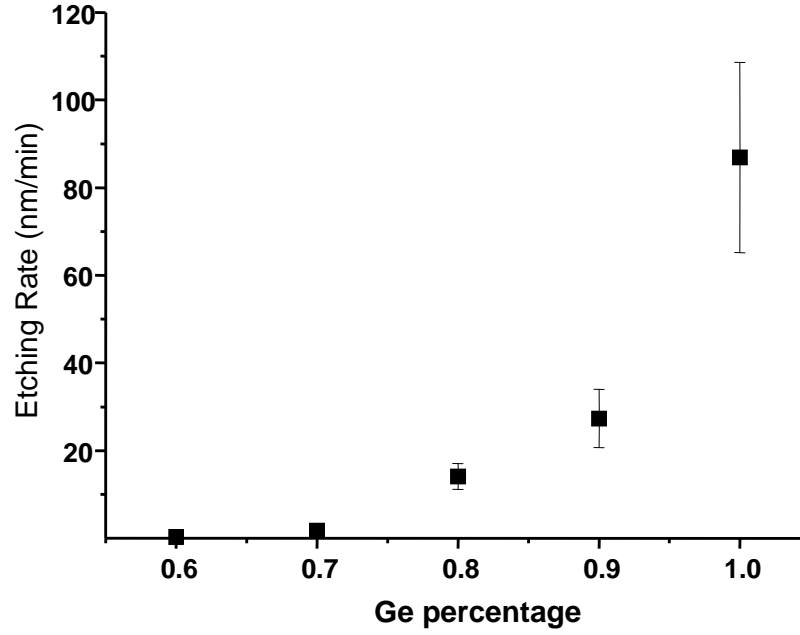
Figure 5.15: Etching rate of (31 H_2O_2:69 H_2O) at room temperature versus Ge content, measured for planar Si_xGe_{1-x} samples. Data courtesy of G. Katsaros [106].

ual islands and to correlate this with the island shape and size, is represented by selective chemical etching. Basically this method consist in exposing an AB binary alloyed sample to a reactive agent that has a much higher etching rate for element A than for element B. The structures that are left over after the etching have a strong B-enrichment and, in case of a 3D island, can be interpreted as the regions with the highest B content [105].

As selective etchant in our experiments we chose hydrogen peroxide diluted in water (31 H_2O_2:69 H_2O) since it has been shown that this solution has the right selectivity for the Ge/Si system [105, 106]. Figure 5.15 quantitatively shows the etching rate of a GeSi alloy as a function of the Ge content. Recently, selective etching experiments based on this solution, demonstrated that nominally pure Ge/Si(001) pyramids have highly Si intermixed corners, whereas the edges, the apex and the center are Ge rich (an average Ge concentration of at least 65%$\pm$5% was determined) [105]. Here we apply the same technique to the islands that appear during the pyramid-to-dome transition and whose thorough structural characterization was given
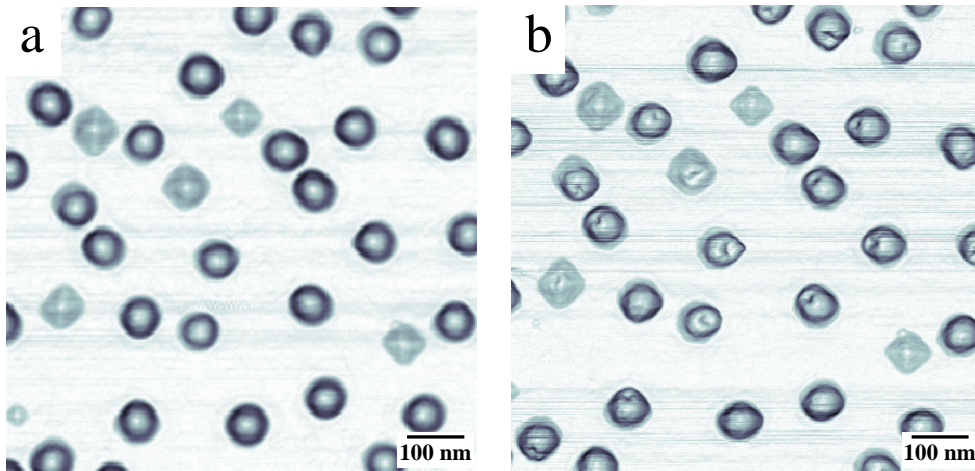
Figure 5.16: AFM topographic images of (a) a 6 ML Ge/Si(001) sample grown at $560°C$ and annealed at the same temperature for 600 sec, and (b) the same sample after being dipped in diluted hydrogen peroxide for 5 min. Notice that the two images show *exactly* the same area of the sample. The colorscale corresponds to the local surface slope.

in the first part of this chapter.

The experiments were conducted as follows: samples as those analyzed in Fig. 5.3b were removed from the UHV chamber and softly scratched with a diamond tip, with the intention of using these marks as a positioning reference before and after the etching experiments. Then AFM measurements were done close to the scratched regions before dipping the sample in the H_2O_2 solution for 10 minutes at room temperature. The sample was successively dried and positioned under the optical microscope integrated into the AFM apparatus. By means of two x-y positioning micrometric screws, with the help of the reference scratches and a huge dose of patience, it was possible to find exactly the same area scanned before the etching.

Figure 5.16 shows a typical result of these experiments. In (a) an AFM image of the pristine sample (6 ML Ge deposited on Si(001) at $560°C$, annealed at the same temperature for 600 sec) is presented. Although the AFM resolution is much lower that that of the STM, the coexistence of different types of islands at different stages of the pyramid-to-dome transition can still be recognized. Fig. 5.16b corresponds to the surface morphology of the same region after the etching procedure. The formation of
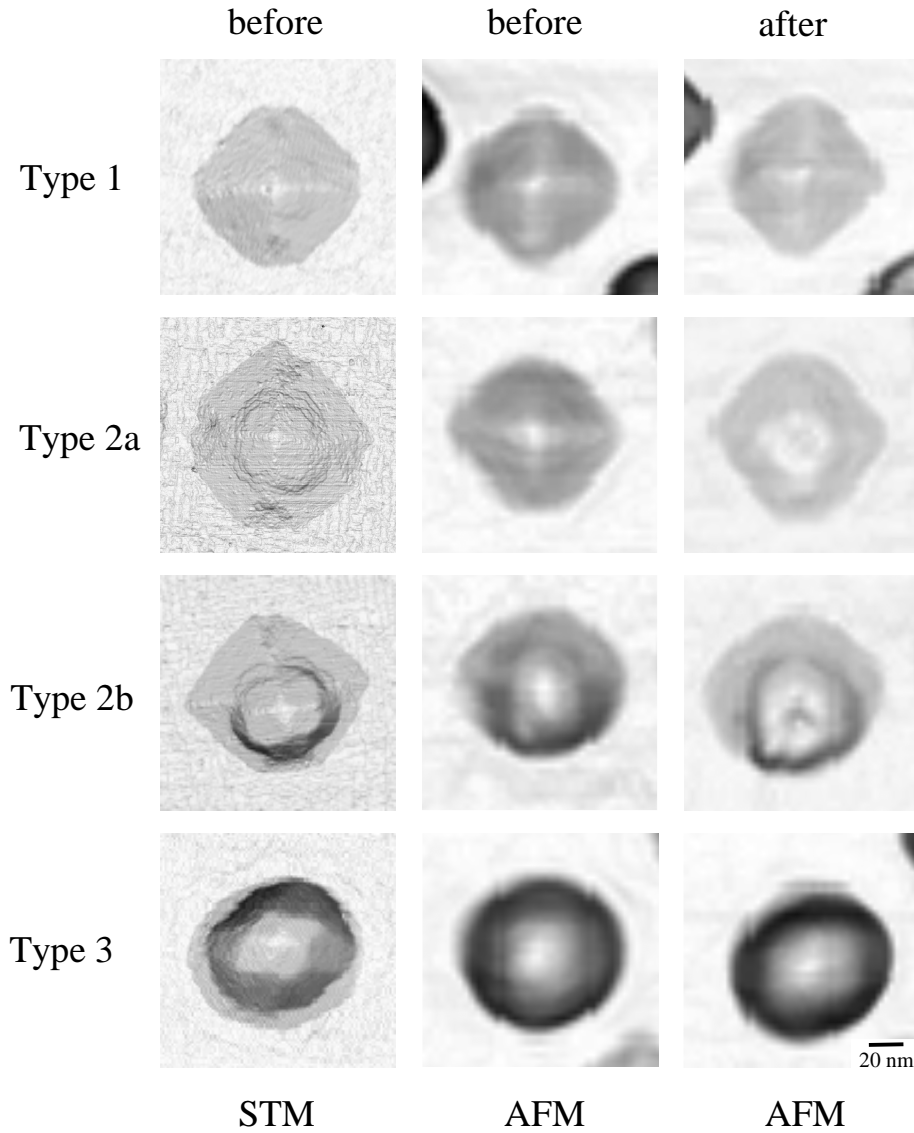
Figure 5.17: Correlation between morphology and etching behavior. Left column: reference STM images for better identifying the island type. Middle and right column: AFM images of the same dot before and after etching, respectively. (see text.)

small dips on most of the islands is clearly seen, being a sign that material has been removed from these regions. This sample has been etched for 10 minutes, but longer etching times did not produce any relevant morphological modification, indicating that the remaining surface profile cannot be further eroded by the H_2O_2 solution.

The correlation between the composition of an island and the morphological stage

it has reached within the pyramid-to-dome transition, can be deduced from Fig. 5.17. For each island type, representative AFM images of the same dot are shown before (middle column) and after the etching (right column). The high resolution STM images in the left column are only used as a reference for better identifying the island morphology (they correspond to similar but not identical dots).

A straightforward interpretation can be given to the etching results of the transition islands, see Figs. 5.17b-d. In fact, as we have seen in Section 5.4, the upper part of the pyramids is a preferential adsorption site for a Ge atom. On the contrary, the regions close to the pyramid base, having a lattice parameter similar to that of the Si substrate, represent favorable sites for Si atoms. As a consequence a SiGe flux arriving from the substrate will distribute unevenly on the pyramid, with a Ge accumulation on the top and a corresponding Si one at the base. We notice that this is produced by the same energy minimization arguments that explain the cap formation, and therefore the pyramid-to-dome transition (see Section 5.4).

The interpretation of the results for regular pyramid and domes (Figs. 5.17 and e) is on the other hand much less intuitive. Further experiments done with etchants of different selectivity should be performed in order to get a more detailed picture of all the full compositional map of the islands. In fact, it should be considered that the etching of an island stops as soon as a region with a certain critical Si content is exposed (the same Si content that determines the selectivity of the etchant, ~ 40 % in the case of 31 H_2O_2:69 H_2O, see Fig. 5.15). Therefore, hypothetical Ge-rich cores located in the central part of the islands could only be revealed by a less selective etchant, able to "perforate" the outer Si-rich shell.

Nevertheless, some hypotheses can be made on the reason why both small pyramids and large, fully developed domes, do not show any signature of erosion. In the latter case, we have to recall that the depth of the trenches formed around the islands base scales with the islands size, so that while the islands increase their dimensions, the material removed from the island vicinity becomes richer in Si. If we assume that the material removed by forming the trench is mainly arranged on the island itself and that the islands increase their size by a sequential overgrowth (as already stated

in section 5.1), then the outermost composition of an island should have a Si content that increases with the island size. This would therefore produce an outer Si-rich shell in the case of large domes that hinder the etching as experimentally observed in Fig. 5.17e.

In the case of smaller pyramids the absence of etching has to be produced by other causes, since this islands are surrounded only by small and shallow trenches (see Fig. 5.11a). A possible explanation could be that, for pyramids smaller than a certain size the effect of separation between Ge and Si atoms is less pronounced. In other words, the difference in absorption energy that a Ge atom experiences between the top and the base of a small island is still too small for producing a sensible segregation of Ge in the upper regions. This segregation only happens for larger islands, as demonstrated by Figs. 5.17b-d, while a more uniformly intermixed SiGe composition characterizes smaller pyramids.

Of course the effect of Ge segregation will gradually increase with the island size and the question whether an island is big enough to produce a Ge segregation that is detectable in an etching experiment, depends on the selectivity of the etchant. Therefore also here the experiments with a less selective etchant would be extremely helpful in determining the exact island composition.

Chapter 6

Outlook: Nanoholes

6.1   Introduction

This last chapter is devoted to a research topic that did not constitute the main focus of my work and that I pursued during the last part of the PhD period. The data that are described here, represent only preparatory measurements and first attempts in the direction of developing novel semiconductor-based nanostructures. Nevertheless, already our preliminary results, demonstrate that these systems bear a huge potential and might become extremely attractive both from a fundamental and an application-oriented point of view.

All the structures presented in the following rely on a novel fabrication approach based on the formation of self-organized QDs in the SK mode. This new method was recently developed by the MBE group of the Max Planck Institute in Stuttgart and combines the overgrowth and the *in-situ* etching of large InAs QDs, leading to the formation of holes with depths of a few nm. These nanoholes are then used as templates for the formation of various types of nanostructures, depending on the way they are further functionalized.

The typical procedure for the formation of the nanoholes starts with the growth of large InAs/GaAs(001) QDs (Fig. 6.1a), nominally identical to those investigated in Chapter 3. Immediately after their formation, the islands are overgrown with 10 nm GaAs (around 35 MLs) deposited at a rate of 0.6 ML/s, while simultaneously
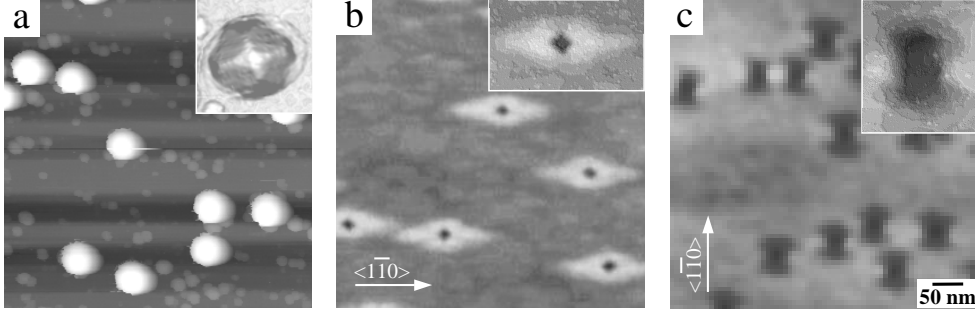
Figure 6.1: Different processing steps followed for the creation of nanoholes. Large images correspond to AFM images, insets to high resolution STM topographies of single structures. The insets are all at the same scale. (a) Large InAs islands before overgrowth. (b) Diamond structures formed after capping the islands with 30 nm GaAs while simultaneously ramping the temperature from 470°C to 500°C. (c) Nanoholes formed after exposing the diamonds to AsBr$_3$.

a temperature ramp (from 470°C to 500°C) is applied to the sample. Figure 6.1b shows the surface morphology after this processing step: shallow structures with a rhombus base elongated in the $\langle 1\bar{1}0 \rangle$ direction and with a hole at their center (we call them "diamonds") are formed on top of each pristine (large) QD. The overgrowth procedure is not much different to that analyzed in Chapter 4 for the case of high deposition rates, and therefore it is not surprising that the resulting surface structures are similar to the camel humpbacks shown in Fig. 4.7d. The shallower aspect ratio of the diamonds and the fact that the central hole is completely encompassed, are most probably the result of an enhanced surface diffusion induced by the temperature ramp. In passing we notice that the diamonds are, on their turn, very similar to the quantum-ring structures that have been reported after the overgrowth and the annealing of similarly large InAs QDs [108]. These systems attracted a large interest since they display topology-induced quantum effects, as e.g. Aharonov-Bohm type oscillation in the ground state energy the single-particle states [109, 110]. Even if a final statement should be based on stronger evidence, we believe that arguments similar to those presented in Section 4.2.2 can be used for explaining the formation of the quantum rings.

If the diamond structures are exposed to an AsBr$_3$ atmosphere at a substrate temperature of 500°C, they evolve into "bow-tie" shaped holes, as seen in Fig. 6.1c. The holes are elongated in the $\langle 110 \rangle$ direction and their depth, typically in the 5 nm range, can be precisely tuned by changing the AsBr$_3$ exposure time [111]. These peculiar structures form because of the selective etching properties of AsBr$_3$ that is known to preferentially remove strained GaAs [112]. As a consequence, the shape of the holes reflects the anisotropic strain fields induced by the buried island in the GaAs cap. As demonstrated by high-resolution STM data, the surface surrounding the holes is characterized by a c(4x4) reconstruction, indicating a pure GaAs(001) composition (see also appendix A).

The structures in Fig. 6.1c represent optimal templates for the realization of new nanostructures. In the following, three envisaged applications will be shortly presented together with the first results on their characterization. Nevertheless the number of different possibilities is almost unlimited and in principle depends only on the different materials that are used for filling the holes.

6.2 Nanoholes functionalization

6.2.1 Hybrid magnetic-semiconductor nanostructures

A first example of the hole functionalization, is represented by their coverage with a thin Fe layer. The Fe deposition is done at room temperature, in order to avoid As/Fe intermixing. It is known that this intermixing is responsible for the formation of a so-called magnetic dead layer that deteriorates the magnetic and spin injection properties of the Fe/GaAs(001) interface. The resulting surface morphology is shown in Figs 6.2a and b. In the larger scan (Fig. 6.2a) it is clearly seen that the shape of the hole is preserved, while higher resolution images (Fig. 6.2b) demonstrate that small 3D islands ($\sim$ 4 nm in diameter) are formed and cover the whole sample surface, inclusive the inner part of the holes. This 3D growth mode is typical for the initial stages of Fe deposited on flat GaAs(001) [114, 115], but has also been reported for the homoepitaxial growth of Fe on Fe(001) [116].
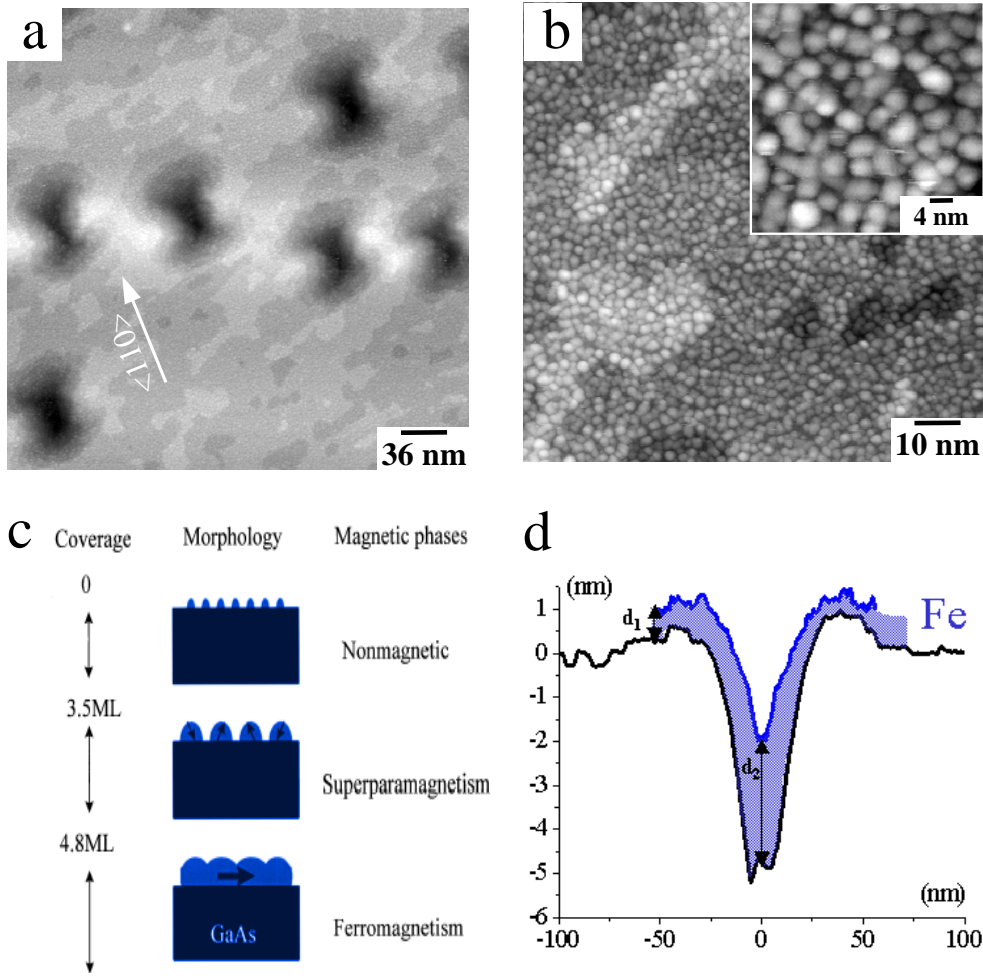
Figure 6.2: STM images of a nanohole sample after the deposition of a thin Fe film at room temperature. (a) The shape of the holes is preserved. (b) 3D islands are formed on the whole sample surface. (c) Evolution of the magnetic properties of the Fe/GaAs(001) as a function of the Fe thickness (data adapted form [115]). (d) $\langle 1\bar{1}0 \rangle$ linescan on the nanoholes structure, before (black line) and after (blue line) the deposition of the Fe film. The Fe thickness on top of the holes d_2 is higher than above flat regions between them d_1.

The Fe/GaAs(001) experiments [114, 115] also demonstrated that a transition from a paramagnetic through a superparamagnetic to a final ferromagnetic phase occurs with increasing amounts of deposited iron. A critical thickness of 4.8 ML of Fe was evaluated for the latter transition, as schematically illustrated in Fig. 6.2c. Unfortunately, at present it is not possible to calibrate the deposition flux in our

STM chamber, where the Fe overgrowth experiments were done (the monitoring of mass deposition will soon be implemented). Therefore we are not able to precisely state the thickness of the deposited iron film. Nevertheless, linescans taken along the $\langle 1\bar{1}0 \rangle$ direction indicate that the depth of the nanoholes decreases after Fe deposition (see Fig. 6.2d). This means that, whatever its absolute values is, the thickness of the Fe film on top of the nanoholes (d_2) is larger than on the flat surface (d_1), i.e. $d_2 > d_1$. Now, if one was able to choose the total amount of deposited Fe so that $d_1 < 3.5$ and $d_2 > 4.8$, following the phase transition in Fig. 6.2c, it would end up with nanometer-sized ferromagnetic islands immersed in a superparamagnetic sea. Moreover if shallower nanoholes were produced (this is possible by decreasing the AsBr$_3$ exposure time), the pristine covered InAs QDs would not be etched, but still present beneath the holes. Therefore, the Fe overgrowth would lead to the formation of ferromagnetic entities located directly (and exclusively) on top of the capped InAs QDs, which could open the way to a focused injection of spin-polarized charge carries.

Recently, the room temperature injection of spin-polarized electrons has been demonstrated in a light emitting diode [117]. The active region of those heterostructures was composed by several InGaAs quantum wells sandwiched between two GaAs spacer layers and a ferromagnetic Fe layer on top for spin alignment. The preliminary measurements shown here suggest that our proposed approach could have potential applications in the development of similar spin sensitive devices, in which the active region is composed by layers containing QDs. Further experiments and further growth schemes will be investigated and tested.

6.2.2   Self-assembly of inverted GaAs/AlGaAs QDs

In a way, the most natural functionalization of the nanoholes is obtained by covering them with further semiconductor layers. In collaboration with the MBE group of our Institute, we investigated a fabrication scheme for 3D GaAs QDs that uses nanoholes as starting template (Fig 6.3a). First, an AlGaAs layer is deposited on the nanoholes at 500 C, which is a low enough temperature to preserve the holes shape and avoid intermixing as demonstrated by Figs. 6.3b and c. Thereafter GaAs is grown at
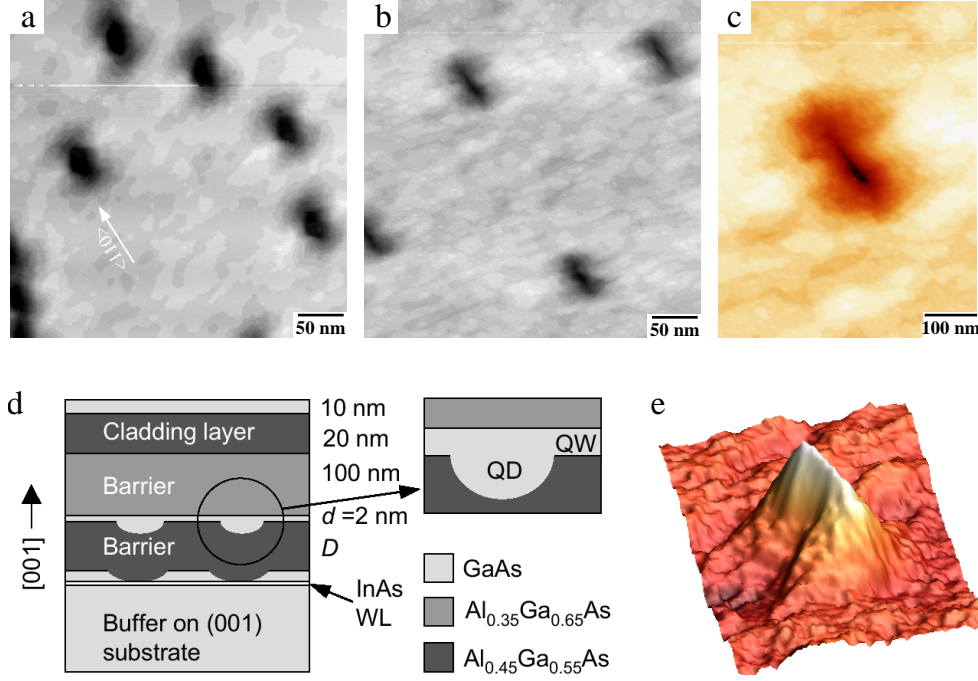
Figure 6.3: STM images showing the different steps followed for the creation of inverted GaAs QDs. (a) Nanoholes before and, (b) after the coverage with AlGaAs. (c) High resolution of a single AlGaAs-capped nanohole. (d) Schematic representation of the complete heterostructure used for (μ-PL) measurements. (e) 3D representation of the inverted GaAs dots. The image is obtained as the "negative" of Fig. 6.3(c).

the same temperature and annealed for 2 minutes. This results in the spontaneous recovery of an atomically flat surface, indicating that the holes are now completely filled with GaAs. An AlGaAs cap is then deposited in order to provide a full electronic confinement and finally a cladding and a passivation layer are added to complete the heterostructure [118] (see schematic representation in Fig 6.3d).

The three-dimensional GaAs QDs are thus formed as inverted islands by the filling of the AlGaAs-terminated structures shown in Figs. 6.3b and c. Several benefits are linked to this growth methodology, first of all the possibility of producing GaAs/AlGaAs QDs based on a self-organized technique. This can in fact not be done by means of the usual SK growth mode, because of the almost perfect match of lattice parameters. On the other hand, this system is extremely interesting since the
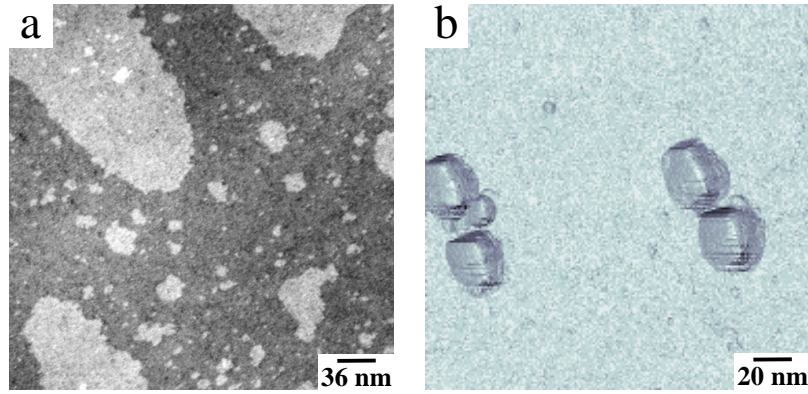
Figure 6.4: STM images of a nanohole sample after being covered with: (a) 0.8-1.4 ML of InAs, the surface becomes atomically flat surface, and (b) 1.6 ML of InAs, pairs of islands, so called quantum dot molecules, are formed. (c) 3D representation of the same image.

grown material is ideally unstrained and sharp interfaces with reduced intermixing can be obtained. Moreover, the shape of the QDs is simply the inverse shape of the AlGaAs-covered nanoholes and can therefore be determined with high precision by means of STM (see Fig. 6.3e). The precise morphological information, the chemical purity and the virtual absence of stress, make these QDs also an ideal subject for theoretical calculations of their electronic properties. Indeed, by taking as input the nominal layer compositions and the QD geometry measured by STM, it was possible to calculate the optical properties of these system and to successfully compare them with single-dot micro-photoluminescence (μ-PL) measurements [118].

6.3 Quantum dot molecules

In this final section we will review the results obtained by re-growing the nanoholes with InAs, a procedure first proposed by the MBE group of the Max Planck Institute in Stuttgart [119]. Fig. 6.4 shows the surface evolution as a function of the amount of deposited InAs: after the growth of 0.8-1.4 ML, the sample becomes atomically flat (see Fig. 6.4a) and is characterized by a (1x3) reconstruction that is typical for an $In_xGa_{1-x}As$ composition with x > 0.3). This reconstruction covers the entire surface

and no remaining morphological fingerprint of the nanoholes is observed. Neverthe-less, only small amounts of further deposited InAs (total amount 1.6 ML), induce the formation of islands couples, what we call quantum dot molecules (QDMs), see Fig. 6.4b and c. The density of these structures correlates, within the experimental error, with the density of the initial QDs and nanoholes, implying that they develop on top of covered holes [119]. The QDMs are aligned in the $\langle 1\bar{1}0 \rangle$ direction, show a small depression at their center and the dots by which they are composed present similar features to the small free standing InAs QDs that we described in Chapter 3. They have an hexagonal base and probably are composed by (137) facets. A pre-cise determination of their structure will be the subject of future investigations. Also their growth mechanism is still not completely clear and neither is the reason why the number of islands formed around a single hole can be tuned by acting on the growth parameters (up to 6 QDs could be obtained in this way [119]). The clarification of all these still open questions will strongly benefit from a systematic atomic-resolution STM study.

The laterally coupled QDM could be potentially useful in all those applications that require controlled assemblies of paired dots, such as quantum information de-vices [120, 121], quantum cellular automata [122] or transistor-less approaches to computation [123]. The proven atomic-like electronic structure of isolated dots al-lows to speculate that quantum dot molecules could show molecular-like electronic states. Scanning tunneling spectroscopy experiments would be extremely useful for the investigation of this issue. By means of a spatial mapping of the electronic wave function of confined states (similar experiments have been recently performed on single InAs QDs [124]), it will be possible to precisely determinate the electronic structure of these artificial molecules and to correlate it with their local structure.

Summary

The results presented along this thesis invigorate STM as one of the fundamental techniques for performing cutting edge research in the burgeoning field of nanoscience. The outstanding spatial resolution achievable by this technique, allowed to elucidate some of the most meaningful issues concerning the growth and overgrowth processes on the two model semiconductor quantum dot systems InAs/GaAs and Ge/Si, which had remained without a clear and satisfactory explanation during the last years. Some of the most relevant achievements accomplished in this thesis are summarized as follows:

In the first part, based on high resolution STM images, it was possible to determine for first time the shape of large self-organized InAs quantum dots on GaAs(001). The experimental findings are in excellent agreement with recent theoretical predictions of the equilibrium crystal shape of InAs quantum dots, demonstrating that the chosen deposition conditions are close to thermodynamic equilibrium.

A detailed investigation of the InAs QDs overgrowth revealed that the whole covering process is a quite complex phenomenon, where the interplay between thermodynamic and kinetic effects determine the shape evolution of the original islands. It was noticed that the overgrowth proceeds in two different time regime processes: at the beginning of the overgrowth, a flux independent regime in which the dissolution of the uncapped dot is accompanied by a shape transformation, and after certain thickness, a regimen in which the morphological evolution of the growth front is kinetically driven. Through the analysis of STM images was possible to precisely identify the different transition shapes experienced by the dots during the first stages of the overgrowth. Moreover, striking similarities were found between the morpho-

logical transitions occured during the overgrowth of InAs/GaAs and Ge/Si QDs, as well as, in the mechanisms inducing these transformations. A parallel description of the different transition islands, pointing the analogies among them supports this observation.

The postgrowth annealing of Ge QD samples led to the shape transition from pyramids to domes. The analysis of STM images taken from these samples revealed that, this morphological transformation is a transient phenomenon in which the pyramids undergo different intermediate shapes before reaching the dome shape. A detailed examination of atomic-resolution images of individual transition islands, allowed to identify the different surface processes driving the shape transition and also to notice that this transformation occurs in a top to bottom way and through the sequential and selective overgrowth of the pyramid islands . A reasoning based on first principle calculations, semiempirical and molecular dynamics simulations, provided the frame for understanding how some of the surface processes observed along this transformation were originated. The technique of selective chemical etching was used in order to determine the island composition at the various stages of the transition. The chemical composition appears to be highly non-uniform with a Si/Ge intermixing that depends on the shape and the size of the islands. Contrarily to what is commonly believed, during the transition the dome-like parts of the islands show a higher Ge composition than the pyramid-like ones.

In the last part of this thesis, a new method for the fabrication of nanostructures was described. This method consists in the *in-situ* etching of diamond nanostructures formed after large InAs QDs are overgrown, that lead to the formation of holes with depths of a few nm. These holes are functionalized in different way depending on the material type they are filled with, or used as nanotemplates for the formation of other nanostructures. Our preliminary results demonstrate that structures obtained by this method bear a huge potential and might become extremely attractive both from a fundamental and an application-oriented point of view.

Appendix A

In this appendix, we will analyze the evolution of the flat regions that separate the QDs during the capping with GaAs. This analysis is restricted to the QD samples that were overgrown at low rate (0.008 ML/s) with GaAs amounts from 1 to 11 ML (the same samples shown in Fig. 3.1), and is performed by means of high resolution STM.

Figure A.1 shows a representative STM image of the surface between uncapped QDs, that were grown by depositing 1.8 ML of InAs on GaAs(001) (details about the growth and overgrowth parameters are specified in chapter 3). This surface, also
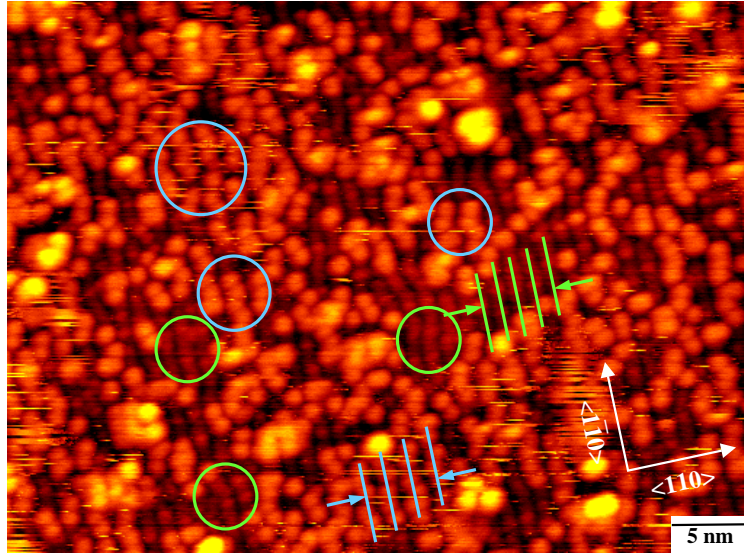
Figure A.1: STM image of the wetting layer separating uncapped QDs. The coexistence of the (2x4) and (1x3) surface reconstructions (blue and green circles respectively) and their respective periodicity, can be identified.
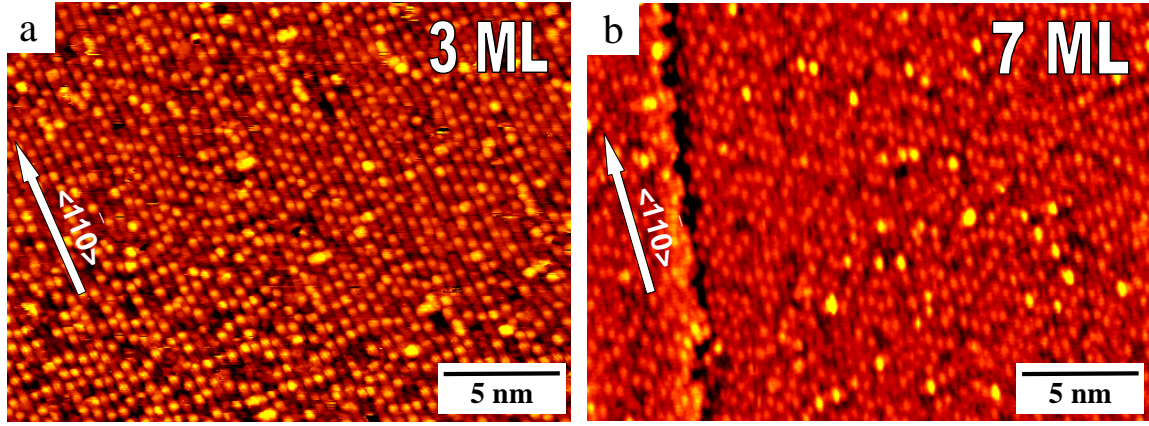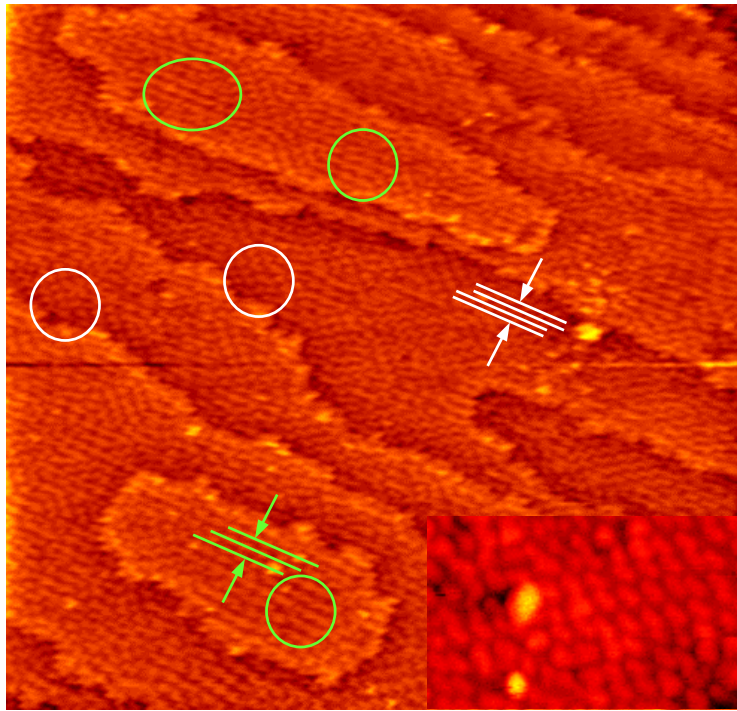
Figure A.2: STM images (35x48 nm^2) of a surface after the overgrowth of 3 and 7 ML of GaAs on a 1.8 ML InAs-GaAs(001) substrate at 460°, the (1x3) surface reconstruction characteristic of the InGaAs alloy is observable in both cases.

called wetting layer (WL) displays the coexistence of two different surface reconstructions, the (2x4) and the (1x3), that are composed by dimer rows that run along $\langle 1\bar{1}0 \rangle$. The (2x4) appears as disordered $\langle 1\bar{1}0 \rangle$ stripes in which the dimers, often arranged in a zig-zag pattern, are separated by ~ 16 $\mathring{A}$ in the $\langle 110 \rangle$ direction. These dimers lie above the plane of the (1x3) reconstruction whose dimers (separation of ~ 12 $\mathring{A}$ along $\langle 110 \rangle$) form continuous and much more regular $\langle 1\bar{1}0 \rangle$) lines.

This latter reconstruction has been reported to be the preferred one for a $In_xGa_{1-x}As$ alloy deposited on GaAs(001) in a wide range of values ,[126]. On the contrary, the (2x4) is known to develop at the experimental temperatures of ∘C, for an almost pure InAs film with (001) orientation [127]. Although 1.8 ML of InAs have been deposited, a coexistence of (1x3) and (2x4) can be observed, instead of a full (2x4). This can be understood in terms of a considerable consumption of the WL material (in particular of InAs) for the formation of the self-organized 3D islands [127].

After covering the samples with GaAs amounts between 1-7 MLs, it is not possible to find any surface regions with the (2x4) surface reconstruction. Conversely, the only visible structure is that corresponding to the (1x3), as shown in Figs. A.2a

Figure A.3: STM image (92x97 nm^2) of a surface after the overgrowth of 11 ML of GaAs on a 1.8 ML InAs-GaAs(001) substrate at 460°, at this point the coexistence of regions where the clean GaAs c(4x4) reconstruction (white circles) is been formed and the (1x3) is observed (green circles). In the inset a close up of the surface shows the "brickwork" pattern characteristic of the c(4x4).

and A.2b. The bright spots that appear in the images are located above the surface plane and, based on recent DFT calculations [], can be interpreted as extra dimers. Only after overgrowing the samples with 11 ML of GaAs, a change in the surface reconstruction is noticed (Fig. A.3a). Domains with the characteristic "brickwork" pattern of the c(4x4) surface reconstruction of GaAs(001) are formed and coexist with (1x3) regions, indicating that a further transition in the surface reconstruction has occurred. Finally, after depositing 15 ML of GaAs, the c(4x4) reconstruction, characteristic of a pure GaAs(001) surface at temperatures ¡ 500∘C, covers the whole surface, see Fig. A.3b.

This sequence of surface reconstruction transformations can be interpreted as re-

sulting from the segregation of In that is a well known effect happening during the earliest stages of the MBE growth of III-V compound heterostructures and leads, for example, to the formation of non-ideal heterojunction interfaces. This phenomena has been observed during the growth of several semiconductor alloys like AlAs on GaAs (Ga segregation), GaSb on AlSb (Al segregation) and GaAs on InAs (In segregation), for citing only some examples [128, 129]. In particular, for the GaAs/InAs(001) system it has been shown that at substrate temperatures around 460°C, the probability that In segregation occurs is very high [72]. This occurs by means of atomic exchange processes between freshly deposited Ga and In substrate atoms and is driven by the lower surface energy of In in respect to Ga. The result is an In-rich film "floating" on the surface [130] and a corresponding Ga incorporation into the subsurface layers.

In our experiments, the initial amount of deposited InAs acts as a finite reservoir of atoms available for the exchange process. During GaAs overgrowth, these are promoted onto the growing interface with a probably ¡ 1, implying that the surface In concentration decreases with increasing the width of the GaAs cap [72]. The Indium atoms are therefore characterized by a certain segregation length that depends on the parameters used during the overgrowth. In our case this corresponds to ~ 11 ML, since only after this cap thickness, the In concentration becomes low enough to allow the formation of pure GaAs c(4x4) domains. This is in agreement with similar values for the indium segregation precedently reported by Belk *et al.* [126]. The gradual reduction of the In content in the surface layer is reflected in the surface reconstruction transformations from a (2x4) through (1x3) to a final c(4x4).

Bibliography

[1] P. M. Petroff, A. Lorke, and A. Imamoglu, Phys. Today 54, 46 (2001).

[2] S. Fafard, K. Hinzer, S. Raymond, M. Dion, J. McCaffrey, and S. Charbonneau, Science 274, 1350 (1997).

[3] X. Huang, A. Stintz, C.P. Hains, G.T. Liu, J. Chen, and K.J. Malloy, Photon. Technol. Lett. 12, 227 (2000).

[4] H. Saito, K. Nishi, I. Ogura, S. Sugou, and Y. Sugimoto, Appl.Phys. Lett. 69, 3140 (1996).

[5] G. Park, O. B. Shchekin, S. Csutak, D. L. Huffaker, and D. G. Deppe, Appl. Phys. Lett. 75, 3267 (1999).

[6] D. P. DiVincenzo, Science 270, 255 (1995).

[7] A. Imamoglu, D. D. Awschalom, G. Burkard, D. P. DiVincenzo, D. Loss, M. Sherwin, and A. Small, Phys. Rev. Lett. 83, 4204 (1999).

[8] G. D. Sanders, K. W. Kim, and W. C. Holton, Phys. Rev. B 61, 7526 (2000).

[9] Z. Yuan, B. E. Kardynal, R. M. Stevenson, A. J. Shields, C. J. Lobo, K. Cooper, N. S. Beattie, D. A. Ritchie, and M. Pepper, Science 295, 102 (2000).

[10] M. Pelton, C. Santori, J. Vukovi, B. Zhang, G. S. Solomon, J. Plant, and Y. Yamamoto, Phys. Rev. Lett. 89, 233602 (2002).

[11] S. Benjamin, Science 290, 2273 (2000).

[12] J. Kim, O. Benson, H. Kan, and Y. Yamamoto, Nature 397, 500 (1999).

[13] G. Brassard, N. Lutkenhaus, T. Mor and B. C. Sanders, Phys. Rev. Lett. 85, 1330 (2000).

[14] M. Reed, Sci. Am. 268, 98 (1993).

[15] D. J. Eaglesham and M. Cerullo, Phys. Rev. Lett. 64, 1943 (1990).

[16] G. Springholz, V. Holy, M. Pinczolits, and G. Bauer, Science 282, 734 (1998).

[17] M. Tomitori, K. Watanabe, M. Kobayashi, and O. Nishikawa, Appl. Surf. Sci. 76/77, 322 (1994).

[18] D. Leonard, M. Krishnamurthy, C. M. Reaves, S. P. Denbaars, and P. M. Petroff, Appl. Phys. Lett. 63, 3203 (1993).

[19] M. Pinczolits, G. Springholz, and G. Bauer, Appl. Phys. Lett. 73, 250 (1998).

[20] K. Alchalabi, D. Zimin, G. Kostorz, and H. Zogg, Phys. Rev. Lett. 90, 026104 (2003).

[21] H. Lee, J. A. Johnson, M. Y. He, J. S. Speck, and P. M. Petroff, Appl. Phys. Lett. 78, 105 (2001).

[22] H. J. Güntherodt and R. Wiesendanger, Scanning Tunneling Microscopy I/II, Springer Series in Surface Science, Springer (1994).

[23] O. Leifeld, Thesis, EPFL (1999).

[24] O. Leifeld, B. Müller, D. A. Grützmacher, and K. Kern, Appl. Phys. A 66, S993 (1998).

[25] K. Besocke, Surf. Sci. 181, 145 (1987).

[26] R. Kliese, B. Röttger, D. Badt, and H. Neddermeyer, Ultramicroscopy. 42-44, 824 (1992).

[27] L. Andersohn and U. Köhler, Surf. Sci. 284, 77 (1993).

[28] M. Udagawa, Y. Umetani, H. Tanaka, M. Itoh, T. Uchiyama, Y. Watanabe, T. Yokotsuka, and I. sumita, Ultramicroscopy. 42-44, 946 (1992).

[29] J.R.Engstrom and Thomas Engel, Phys. Rev. B. 41, 1038 (1990).

[30] Ludeke and A. Koma, Phys. Rev. Lett. 34, 817 (1975).

[31] W. Ranke and K. Jacobi, Prog. Surf. Sci. 10, 1-52 (1980).

[32] T. Kaneko, T. Saeger, and K. Eberl, Materials Research SocietyVol. 405: Surface/Interface and Stress Effects in Electronic Material Nanostructures, 1996, edited by S. M. Prokes, R. C. Cammarata, K. L. Wang, and A. Christou, pp. 67-71, Materials Research society (Pittsburgh, PA, 1996).

[33] K. Brunner, K. Eberl, W. Winter, and N. Y. Jin-Phillipp, Appl. Phys. Lett. 69, 91 (1996).

[34] R. Stalder, H. Gübeli, H. von Känel, and P. Wachter, Rev. Sci. Instrum. 63, 1676 (1992).

[35] G. Park, O. B. Shchekin, D. L. Huffaker, and D. G. Deppe, Appl. Phys. Lett. 73, 3351 (1998).

[36] S. Sauvage, P. Boucaud, F. H. Julien, J. M. Gerard, and V. Thierry-Mieg, Appl. Phys. Lett. 71, 2785 (1997).

[37] M. J. da Silva, A. A. Quivy, S. Martini, T. E. Lamas, E. C. F. da Silva, and J. R. Leite Appl. Phys. Lett. 82, 2646 (2003).

[38] D. Bimberg and N. Ledentsov , J. Phys.: Condens. Matter. 15, R1063 (2003).

[39] J. Màrquez, L. Geelhaar, and K. Jacobi, Appl. Phys. Lett. 78, 2309 (2001).

[40] P. B. Joyce, T. J. Krzyzewski, P. H. Steans, G. R. Bell, J. H. Neave, and T. S. Jones, Surf. Sci. 492, 345 (2001).

[41] Y. Hasegawa, H. Kiyama, Q. K. Xue, and T. Sakurai, Appl. Phys. Lett. 72, 2265 (1998).

[42] R. Murray, D. Childs, S. Malik, P. Siverns, C. Roberts, J. M. Hartmann, and P. Stavrinou, Jpn. J. Appl. Phys. 38, 528 (1999).

[43] O. G. Schmidt, S. Kiravittaya, Y. Nakamura, H. Heidemeyer, R. Songmuang, C. Müller, N. Y. Jin-Phillipp, K. Eberl, H. Wawra, S. Christiansen, H. Gräbeldinger, and H. Schweizer, Surf. Sci. 514, 10 (2002).

[44] H. Heidemeyer, S. Kiravittaya, C. Müller, N. Y. Jin-Phillipp, and O.G. Schmidt, Appl. Phys. Lett. 80, 1544 (2002).

[45] J. G. Belk, J. L. Sudijono, D. M. Holmes, C. F. McConville, J. L. Sudijono, T. S. Jones, and B. A. Joyce, Surf. Sci. 365, 735 (1996).

[46] F. Patella, M. Fantoni, F. Arciprete, S. Nufris, E. Placidi, and A. Balzarotti, Appl. Phys. Lett. 78, 320 (2001).

[47] H. Saito, K. Nishi, and S. Sugou, Appl. Phys. Lett. 74, 1224 (1999).

[48] I. Mukhametzhanov, Z. Wei, R. Heitz, and A. Madhukar, Appl. Phys. Lett. 75, 85 (1999).

[49] S. Kiravittaya, Y. Nakamura, and O. G. Schmidt, Physica E 13, 224 (2002).

[50] H. Heidemeyer, S. Kiravittaya, C. Müller, N. Y. Jin-Phillipp, and O. G. Schmidt, Appl. Phys. Lett. 80, 1544 (2002).

[51] M. A. Lutz, R. M. Feenstra, P. M. Mooney, J. Tersoff and J. O. Chu, Surf. Sci. 316, L1075 (1994).

[52] A. Rastelli and H. von Känel, Surf. Sci. 515, L493 (2002).

[53] B. A. Joyce, T. S. Jones, and J. G. Belk, J. Vac. Sci. Technol. B 16, 2373 (1998).

[54] N. Moll, M. Scheffler, and E. Pehlke, Phys. Rev. B 58, 4566 (1998).

[55] N. Moll, A. Kley, E. Pehlke, and M. Scheffler, Phys. Rev. B 54, 8844 (1996).

[56] E.Pehlke, N. Moll, A. Kley, and M. Scheffler, Appl. Phys. A 65, 525 (1997).

[57] N. Moll, M. Scheffler, and E. Pehlke, Phys. Rev. B 58, 4566 (1998).

[58] P. Kratzer, private communication.

[59] Q. K. K. Liu, N. Moll, M. Scheffler, and E. Pehlke, Phys. Rev. B 60, 17008
      (1999).

[60] S. Hirose, A. Yoshida, M. Yamaura, and H. Munekata, Appl. Phys. Lett. 74, 964
      (1999).

[61] P. B. Joyce, T. J. Krzyzewski, G. R. Bell, T. S. Jones, E. C. Le Ru, and R.
      Murray, Phys. Rev. B 64, 235317 (2001).

[62] K. Zhang, Ch. Heyn, W. Hansen, Th. Schmidt, and J. Falta, Appl. Surf. Sci.
      175-176, 606 (2001).

[63] Q. Xie, A. Madhukar, P. Chen, and N. P. Kobayashi, Phys. Rev. Lett. 75, 2542
      (1995).

[64] J. Tersoff, C. Teichert, and M. G. Lagally, Phys. Rev. Lett. 76, 1675 (1996).

[65] G. S. Solomon, J. A. Trezza, A. F. Marshall, and J. S. Harris, Phys. Rev. Lett.
      76, 952 (1996).

[66] F. Liu, S. E. Davenport, H. M. Evans, and M. G. Lagally, Phys. Rev. Lett. 82,
      2528 (1999).

[67] R. Songmuang, S. Kiravittaya, and O.G. Schmidt, J Cryst. Growth 249,416
      (2003).

[68] X. W. Lin, J. Washburn, Z. Lilienthal-Weber, E. R. Weber, A. Sasaki, A. Waka-
      hara, and Y. Nabetani, Appl. Phys. Lett. 65, 1677 (1994).

[69] Q. Xie, P. Chen, and A. Madhukar, Appl. Phys. Lett. 65, 2051 (1994).

[70] A. Rastelli, M. Kummer, and H. von Känel Phys. Rev. Lett. 87, 256101 (2001).

[71] J. M. Moison, F. Houzay, F. Barthe, J. M. Gerard, B. Jusserand, I. Massies, and F. S. Turco-Sandroff, J. Cryst. Growth 111, 141 (1991), and references therein.

[72] K. Muraki, S. Fukatsu, Y. Shiraki, and R. Ito, Appl. Phys. Lett. 61, 557 (1992).

[73] A. G. Cullis, D. J. Norris, T. Walther, M. A. Migliorato, and M. Hopkinson, Phys. Rev. B 66, 081305 (2002).

[74] G. J. Salamo, private communication.

[75] I. Daruka, J. Tersoff, and A. L. Barabsi, Phys. Rev. Lett. 82, 2753 (1999).

[76] K. Shiraishi, Appl. Phys. Lett. 60, 1363 (1992).

[77] J. Singh and A. Madhukar Phys. Rev. Lett. 51, 794 (1983).

[78] T. Walther, A. G. Cullis, D. J. Norris, and M. Hopkinson, Phys. Rev. Lett. 86, 2381 (2001).

[79] N. Liu, J. Tersoff, O. Baklenov, A. L. Holmes, and C. K. Shih, Phys. Rev. Lett. 84, 334 (2000).

[80] I. Kegel, T. H. Metzger, A. Lorke, J. Peisl, J. Stangl, G. Bauer, J. M. Garcìa, and P. M. Petroff, Phys. Rev. Lett. 85, 1694 (2000).

[81] J. Ouellette, The industrial physicist 8, 22 (2002).

[82] H. Sakaki, Solid State Commun. 92, 119 (1994).

[83] R. M. Tromp and F. M. Ross, Annu. Rev. Mater. Sci. 30, 431 (2000).

[84] Karl Brunner, Rep. Prog. Phys. 65, 27-72 (2002).

[85] Y.-W. Mo, D. E. Savage, B. S. Swartzentruber, and M. G. Lagally, Phys. Rev. Lett. 65, 1020 (1990).

[86] A. Vailionis, B. Cho, G. Glass, P. Desjardins, D. G. Cahill, and J. E. Greene, Phys. Rev. Lett. 85, 3672 (2000).

[87] G. Medeiros-Ribeiro, A. M. Bratkovski, T. I. Kamins, D. A. A. Ohlberg, and R. S. Williams, Science 279, 353 (1998).

[88] J. A. Floro, E. Chason, and R. D. Twesten, Phys. Rev. Lett. 79, 20 (1997).

[89] A. R. Woll, P. Rugheimer, and M. G. Lagally, IJHSES 12, 45 (2002).

[90] T. I. Kamins, E. C. Carr, R. S. Williams, and S. J. Rosner, J. Appl. Phys. 81, 211 (1997).

[91] F. M. Ross, R. M. Tromp, and M. C. Reuter, Science 286, 1931 (1999).

[92] A. Rastelli, Thesis, University of Pavia (2002).

[93] to be published.

[94] Y. Fujikawa, K. Akiyama, T. Nagao, T. Sakurai, M. G. Lagally, T. Hashimoto, Y. Morikawa, and K. Terakura, Phys. Rev. Lett. 88, 176101 (2002).

[95] P. Raiteri and L. Miglio, Phys. Rev. B 66 , 235408 (2002).

[96] F. Montalenti, private communication.

[97] S. A. Chaparro, Y. Zhang, and J. Drucker, Appl. Phys. Lett. 76, 3534 (2000).

[98] U. Denker, O. G. Schmidt, N. Y. Jin-Philipp, and K. Eberl, Appl. Phys. Lett. 78, 3723 (2001).

[99] P. Raiteri, L. Miglio, F. Valentinotti, and M. Celino, Appl. Phys. Lett. 80, 3736 (2002).

[100] A. van de Walle, M. Asta, and P. W. Voorhees, Phys. Rev. B 67, 041308 (2003).

[101] E. Penev, P. Kratzer, and M. Scheffler, Phys. Rev. B 64, 085401 (2001).

[102] S. P. Nikanorov, Y. A. Burenkov, and A. V. Stepanov, Sov. Phys. Solid State 13, 2516 (1972).

[103] M. Floyd, Y. T. Zhang, K. P. Driver, J. Drucker, P. A. Crozier, and D. J. Smith, Appl. Phys. Lett. 82, 1473 (2003).

[104] Rosei, private communication.

[105] U. Denker, M. Stoffel, and O. G. Schmidt, Phys. Rev. Lett. 90, 196102 (2003).

[106] G. Katsaros, to be published.

[107] R. Magalhes-Paniago, G. Medeiros-Ribeiro, A. Malachias, S. Kycia, T. I. Kamins, and R. S. Williams, Phys. Rev. 66, 245312 (2002).

[108] J. M. Garca, G. Medeiros-Ribeiro, K. Schmidt, T. Ngo, J. L. Feng, A. Lorke, J. Kotthaus, and P. M. Petroff, Appl. Phys. Lett. 71, 2014 (1997).

[109] R. J. Warburton, C. Schflein, D. Haft, F. Bickel, A. Lorke, K. Karrai, J. M. Garcia, W. Schoenfeld, and P. M. Petroff, Nature 405, 926 (2000).

[110] A. Lorke, R. J. Luyken, A. O. Govorov, J. P. Kotthaus, J. M. Garcia, and P. M. Petroff, Phys. Rev. Lett. 84, 2223 (2000).

[111] S. Kiravittaya, R. Songmuang, N. Y. Jin-Phillipp, S. Panyakeow, O.G. Schmidt, J. Cryst. Growth 249, 416 (2003).

[112] H. Schuler, T. Kaneko, M. Lipinski, and K. Eberl, Semicond. Sci. Technol. 15, 169 (2000).

[113] E. M. Kneedler, B. T. Jonker, P. M. Thibado, R. J. Wagner, B. V. Shanabrook, and L. J. Whitman, Phys. Rev. B 56, 8163 (1997).

[114] E. M. Kneedler, B. T. Jonker, P. M. Thibado, R. J. Wagner, B. V. Shanabrook, and L. J. Whitman, Phys. Rev. B 56, 8163 (1997).

[115] Y. B. Xu, E. T. M. Kernohan, D. J. Freeland, A. Ercole, M. Tselepi, and J. A. C. Bland, Phys. Rev. B 40, 890 (1998).

[116] J. A. Stroscio, D. T. Pierce, M. D. Stiles, A. Zangwill, and L. M. Sander, Phys. Rev. Lett. 75, 4246 (1995).

[117] H. J. Zhu, M. Ramsteiner, H. Kostial, M. Wassermeier, H. P. Schönherr, and K. H. Ploog, Phys. Rev. Lett. 87, 016601 (2001).

[118] A. Rastelli, S. Stufler, A. Schliwa, R. Songmuang, C. Manzano, G. Costantini, K. Kern, A. Zrenner, D. Bimberg, and O. G. Schmidt, accepted in PRL (in press).

[119] R. Songmuang, S. Kiravittaya, and O. G. Schmidt, Appl. Phys. Lett. 82, 2892 (2003).

[120] A. Imamoglu, D. D. Awschalom, G. Burkard, D. P. DiVincenzo, D. Loss, M. Sherwin, and A. Small, Phys. Rev. Lett. 83, 4204 (1999).

[121] G. Burkard, G. Seelig, and D. Loss, Phys. Rev. B 62, 2581 (2000).

[122] C. S. Lent, P. D. Tougaw, W. Porod, and G. H. Bernstein, Nanotechnology 4, 49 (1993).

[123] A. O. Orlov, I. Amlani, G. H. Bernstein, C. S. Lent, and G. L. Snider, Science 277, 928 (1997).

[124] M. Morgenstern, J. Klijn, Chr. Meyer, and R. Wiesendanger, Phys. Rev. Lett. 90, 179901 (2003).

[125] P. Kratzer, E. Penev, and M. Scheffler, Appl. Surf. Sci. 216, 436 (2003).

[126] J. G. Belk, C. F. McConville, J. L. Sudijono, T. S. Jones, and B. A. Joyce, Surf. Sci. 387, 213 (1997).

[127] P. B. Joyce, T. J. Krzyzewski, G. R. Bell, B. A. Joyce, and T. S. Jones, Phys. Rev. B 58, R15981 (1998).

[128] C. Raisin, H. Tegmousse, and L. Lassabatere, Vide Couches Minces 41, 241 (1986).

[129] R. A. Stall, J. Zilko, V. S. Swaminathan, and N. Schumaker, J. Vac. Sci. Technol. B 3, 524 (1985).

[130] J. M. Moison, C. Guille, F. Houzay, F. Barthe, and M. Van Rompay, Phys. Rev. B 40, 6149 (1989).

Curriculum Vitae

Name:	Carlos de Jésus Manzano García
Date of birth:	25.11.72, Yucatán, México
Nationality:	Mexican

Education: Bachelor in Computer Sciences (June, 1996)
Faculty of Mathematics,
Free University of Yucatán, Yucatán, México.
Thesis title: "Computational system for the control
and data acquisition of an ESCA/SAM equipment".

M.Sc. Experimental Physics (June, 2000)
CINVESTAV-IPN (Campus Mérida)
Physics Department, Yucatán, México.
Thesis title: "CdS nanostructures deposited by
the laser ablation technique".

Ph.D. thesis at the Swiss Federal Institute of
Technology Lausanne, (Ecolé Polytechnique
Fédérale de Lausanne).

List of publications

M. Dashiell, U. Denker, C. Müller, G. Costantini, C. Manzano, K. Kern, and O. G. Schmidt, Appl. Phys. Lett. 80, 1279 (2002).

C. Costantini, C. Manzano, R. Songmuang, O. G. Schmidt, and K. Kern, Appl. Phys. Lett. 82, 3194 (2003).

A. Rastelli, S. Stufler, A. Schliwa, R. Songmuang, C. Manzano, G. Costantini, K. Kern, A. Zrenner, D. Bimberg, and O. G. Schmidt, accepted in PRL (in press).

G. Costantini, A. Rastelli, C. Manzano, R. Songmuang, O. G. Schmidt, H. v. Känel, and K. Kern (submitted).